Landsat-8, Advanced Spaceborne Thermal Emission and Reflection Radiometer, and WorldView-3 Multispectral Satellite Imagery for Prospecting Copper-Gold Mineralization in the Northeastern Inglefield Mobile Belt (IMB), Northwest Greenland

Amin Beiranvand Pour [1,2,*], Tae-Yoon S. Park [1], Yongcheol Park [1], Jong Kuk Hong [1], Aidy M. Muslim [2], Andreas Läufer [3], Laura Crispini [4], Biswajeet Pradhan [5,6], Basem Zoheir [7,8], Omeid Rahmani [9], Mazlan Hashim [10] and Mohammad Shawkat Hossain [2]

[1] Korea Polar Research Institute (KOPRI**)**, Songdomirae-ro, Yeonsu-gu, Incheon 21990, Korea; typark@kopri.re.kr (T.-Y.S.P.); ypark@kopri.re.kr (Y.P.); jkhong@kopri.re.kr (J.K.H.)

[2] Institute of Oceanography and Environment (INOS), University Malaysia Terengganu (UMT), Kuala Nerus 21030, Terengganu, Malaysia; aidy@umt.edu.my (A.M.M.); shawkat@umt.edu.my (M.S.H.)

[3] Federal Institute for Geosciences and Natural Resources (BGR), Stilleweg 2, 30655 Hannover, Germany; andreas.laeufer@bgr.de

[4] DISTAV– University of Genova – Corso Europa 26, 16132 Genova, Italy; laura.crispini@unige.it

[5] Centre for Advanced Modelling and Geospatial Information Systems (CAMGIS), Faculty of Engineering and Information Technology, University of Technology Sydney, New South Wales 2007, Australia; Biswajeet.Pradhan@uts.edu.au

[6] Department of Energy and Mineral Resources Engineering, Choongmu-gwan, Sejong University, 209 Neungdong-ro Gwangjin-gu, Seoul 05006, Korea

[7] Department of Geology, Faculty of Science, Benha University, Benha 13518, Egypt; basem.zoheir@gmail.com or basem.zoheir@fsc.bu.edu.eg

[8] Institute of Geosciences, University of Kiel, Ludewig-Meyn Str. 10, 24118 Kiel, Germany

[9] Department of Natural Resources Engineering and Management, School of Science and Engineering, University of Kurdistan Hewlêr (UKH), Erbil 44001, Kurdistan Region, Iraq; omeid.rahmani@ukh.edu.krd

[10] Geoscience and Digital Earth Centre (INSTeG), Research Institute for Sustainable Environment, Universiti Teknologi Malaysia, Johor Bahru, Skudai 81310, Malaysia; mazlanhashim@utm.my

* Correspondence: beiranvand.amin80@gmail.com; Tel.: +82-3-2760-5472

Abstract: Several regions in the High Arctic still lingered poorly explored for a variety of mineralization types because of harsh climate environments and remoteness. Inglefield Land is an ice-free region in northwest Greenland that contains copper-gold mineralization associated with hydrothermal alteration mineral assemblages. In this study, Landsat-8, Advanced Spaceborne Thermal Emission and Reflection Radiometer (ASTER), and WorldView-3 multispectral remote sensing data were used for hydrothermal alteration mapping and mineral prospecting in the Inglefield Land at regional, local, and district scales. Directed principal components analysis (DPCA) technique was applied to map iron oxide/hydroxide, Al/Fe-OH, Mg-Fe-OH minerals, silicification (Si-OH), and SiO2 mineral groups using specialized band ratios of the multispectral datasets. For extracting reference spectra directly from the Landsat-8, ASTER, and WorldView-3 (WV-3) images to generate fraction images of end-member minerals, the automated spectral hourglass (ASH) approach was implemented. Linear spectral unmixing (LSU) algorithm was thereafter used to produce a mineral map of fractional images. Furthermore, adaptive coherence estimator (ACE) algorithm was applied to visible and near-infrared and shortwave infrared (VINR + SWIR) bands of ASTER using laboratory reflectance spectra extracted from the USGS spectral library for verifying the presence of mineral spectral signatures. Results indicate that the boundaries between the Franklinian sedimentary successions and the Etah metamorphic and meta-igneous

complex, the orthogneiss in the northeastern part of the Cu-Au mineralization belt adjacent to Dallas Bugt, and the southern part of the Cu-Au mineralization belt nearby Marshall Bugt show high content of iron oxides/hydroxides and Si-OH/SiO2 mineral groups, which warrant high potential for Cu-Au prospecting. A high spatial distribution of hematite/jarosite, chalcedony/opal, and chlorite/epidote/biotite were identified with the documented Cu-Au occurrences in central and southwestern sectors of the Cu-Au mineralization belt. The calculation of confusion matrix and Kappa Coefficient proved appropriate overall accuracy and good rate of agreement for alteration mineral mapping. This investigation accomplished the application of multispectral/multi-sensor satellite imagery as a valuable and economical tool for reconnaissance stages of systematic mineral exploration projects in remote and inaccessible metallogenic provinces around the world, particularly in the High Arctic regions.

1. Introduction

The application of multispectral satellite imagery for mineral prospecting in remote and inaccessible metallogenic provinces is noteworthy for mining companies and the mineral exploration community for reconnaissance stages of systematic exploration projects. Many regions in the High Arctic remain poorly investigated for mineral exploration due to cold climate environments and remoteness, especially the northern part of Greenland containing Zn-Pb and Cu-Au mineralization [1–3]. The visible and near-infrared (VNIR), shortwave infrared (SWIR) and thermal infrared (TIR) bands of multispectral remote sensing data contain unprecedented spectral and spatial capabilities for detecting hydrothermal alteration minerals and lithological units associated with a variety of ore mineralization [4–22]. Numerous investigations successfully used Landsat data series, Advanced Spaceborne Thermal Emission and Reflection Radiometer (ASTER), and the Advanced Land Imager (ALI) multispectral data with moderate spatial resolution for the reconnaissance stages of mineral exploration around the world [23–29].

Landsat-8 carries two-sensors, including the Operational Land Imager (OLI) and the Thermal Infrared Sensor (TIRS). These two instruments collect data for nine visible, near-infrared, shortwave-infrared bands (from 0.433 to 2.290 μm) and two thermal-infrared bands (from 10.60 to 12.51 μm). The OLI bands have a 30 m spatial resolution, while the TIRS have a 100 m spatial resolution, which acquire in 185 km swaths and segmented into 185 × 180 km scenes. The data have a high signal to noise (SNR) radiometer performance, and 12-bit quantization of the data permits measurement of subtle variability in surface conditions [30,31]. High radiometric sensitivity in the TIR bands shows great potential for mapping exposed lithological units in polar regions through variation in temperature as felsic to mafic rocks show a modified response to solar heating due to different mineral compositions [31–33]. ASTER contains three VNIR bands from 0.52 to 0.86 μm with 15-m spatial resolution, six SWIR bands from 1.6 to 2.43 μm with 30-m spatial resolution, and five TIR bands from 8.0 to 14.0 μm with 90-m spatial resolution. Each scene of ASTER cuts 60 × 60 km^2 [34]. Iron oxide/hydroxide, hydroxyl-bearing, and carbonate mineral groups can be detected using VNIR and SWIR bands of ASTER due to diagnostic spectral absorption features of transition elements (Fe^{2+}, Fe^{3+} and REE) in the VNIR region and Al-OH, Mg-OH, Fe-OH, Si-OH, CO_3, NH_4, and SO_4 groups in the SWIR region [35–37]. Discrimination of silicate lithological groups is feasible using TIR bands of ASTER due to different characteristics of the emissivity spectra derived from Si–O–Si stretching vibrations in the TIR region [18,38–41].

The multispectral commercial WorldView-3 (WV-3) sensor contains the highest spatial, spectral and radiation in the VNIR (eight bands with 1.2 m spatial resolution) and SWIR (eight bands with 3.7 m spatial resolution) portions among the multispectral satellite sensors, presently. WV-3 swath width is 13.2 km [42–45]. The VNIR and SWIR bands of WV-3 are worthy of particular attention for inclusive

research related to detailed mineral exploration at district scale, particularly for remote and inaccessible regions in the High Arctic where availability of field data is limited. Recently, some investigations successfully used the VNIR and SWIR bands of WV-3 for mineral exploration and mapping of hydrothermal alteration zones and lithologies [14,19,32,46–49]. These studies established the efficiency of spatial resolution of the WV-3 dataset and emphasized the high capability of the VNIR and SWIR spectral bands as a valuable multispectral remote sensing data for detailed geological mapping and hydrothermal alteration mineral detection at district scale (1:10,000). The integration of multispectral/multi-sensor satellite imagery contains great applicability as a cost-effective tool compared to geophysical and geochemical techniques for mapping hydrothermal alteration minerals and lithological units at regional, local, and district scales in remote and inaccessible metallogenic provinces around the world.

Inglefield Land is an ice-free region (78°N–79°N and 72°30′W–66°W) in northwest Greenland (Figure 1), which contains copper-gold mineralization hosted by garnet-sillimanite paragneiss, orthogneiss, and mafic-ultramafic rocks [1–3,50–52]. A few geological investigations were carried out in Inglefield Land by the Geological Survey of Denmark and Greenland (GEUS) during years 1994 (an airborne geophysical survey) and 1995 (fieldwork geological mapping, mineralization studies, and a regional stream-sediment geochemical survey). A set of thematic maps with digital data in geographic information system (GIS) format were generated using the data acquired from these two field seasons [53,54]. From July to August 1999, fieldwork conducted in Inglefield Land by the GEUS (as part of a multidisciplinary Kane Basin 1999 project) was directed to the exploration of several remarkable gold mineralizations in the northeastern part of the Inglefield Mobile Belt (IMB) [55,56]. Since there is no remote sensing study available for hydrothermal alteration mineral and lithological mapping in the northeastern IMB, this study represents the first investigation on multispectral/multi-sensor satellite imagery for copper-gold prospecting in this region.
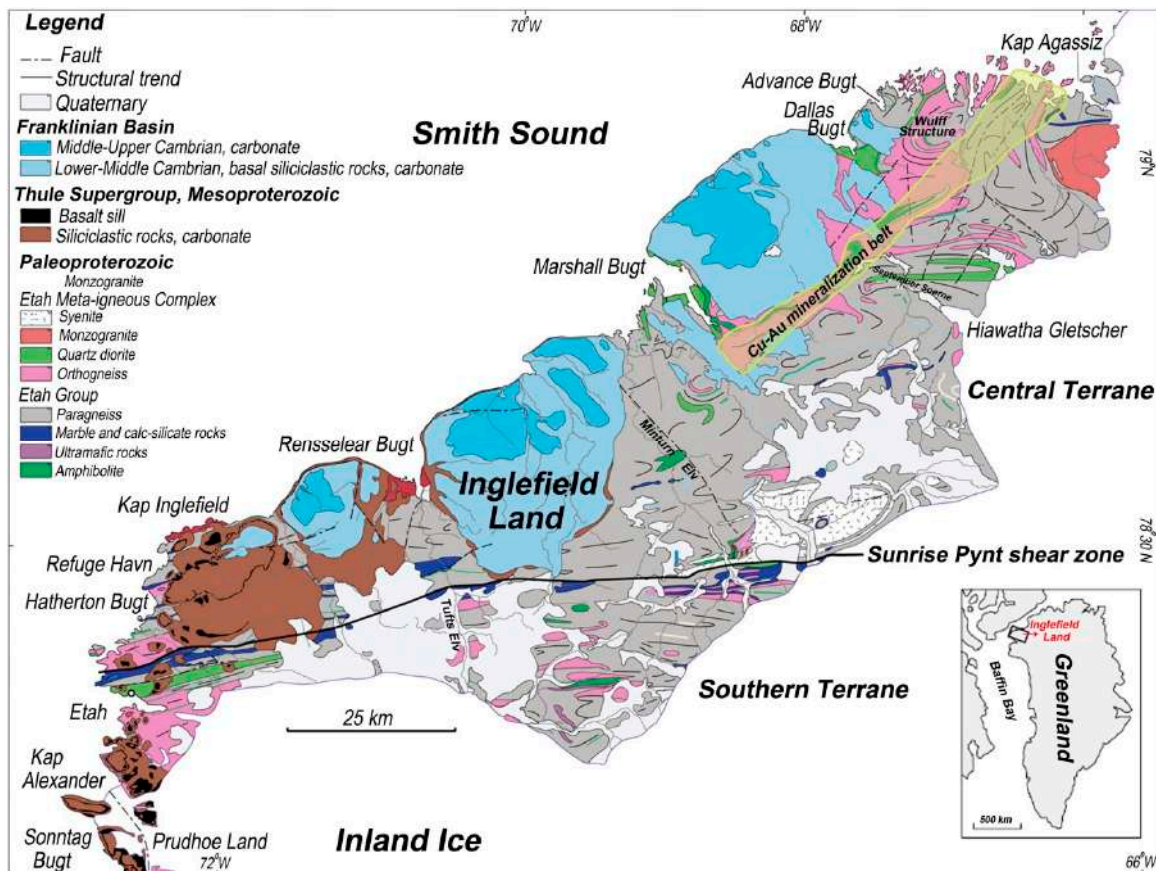

Figure 1. Geological map of the Inglefield Land. Cu-Au mineralized belt in the northeastern part of Inglefield Land shown as a yellow color semi-transparent polygon (modified after [3,42]).

In this research, Landsat-8, ASTER, and WV-3 data were used for hydrothermal alteration and lithological mapping at regional, local, and district scales in the northeastern Inglefield Mobile Belt (IMB), Northwest Greenland (Figure 1). Mineralization in Inglefield Land is characterized by copper-gold ore associated with hydrothermal alteration assemblages such as hematite, jarosite, biotite, sericite, chlorite, epidote, and quartz (silicification), which overprint the altered areas (rust zones) and wall-rocks [2,3]. Typical landscape in the Cu-Au mineralization belt (rust zones) is extensive gossan in hilly terrain and meter-sized pyrrhotite mounds covered by gossan [3]. Consequently, this research has three main purposes: (1) to map hydrothermal alteration minerals associated with copper-gold mineralization in the northeastern IMB using Landsat-8, ASTER, and WV-3 satellite imagery at regional, local, and district scales; (2) to implement specialized/standardized image processing algorithms to VNIR/SWIR/TIR bands of multispectral/multi-sensor satellite imagery that are amendable for mineral detection and analysis; and (3) to establish the applicability of multispectral/multi-sensor satellite imagery as a valuable and cost-effective approach compared to costly geophysical and geochemical techniques for mining companies and the mineral exploration community for reconnaissance stages of systematic exploration projects in remote and inaccessible metallogenic provinces, specifically in the High Arctic regions.

2. Geological Setting of Inglefield Mobile Belt (IMB)

The IMB in northwest Greenland (approximately 7000 km²) (Figure 1) forms the northern boundary of the Rae Craton and continues to the west across the Smith Sound into the Ellesmerian Belt in Canada [57,58]. It consists of quartzo-feldspathic gneisses, meta-igneous, and supracrustal rocks of the Palaeoproterozoic age [59–61]. The IMB is subdivided into two terranes by the E-W striking Sunrise Pynt Shear Zone, including (i) the Central Terrane and (ii) the Southern Terrane (Figure 1) [58]. The Central Terrane comprises of the Etah Group and Etah Meta-igneous Complex [57]. The Etah Group is characterized by paragneiss, marble, calc-silicate rocks, ultramafic rocks, amphiboloite, and quartzite [57–59]. The Etah Meta-igneous Complex consists of orthogneiss, tonalite, diorite, granodiorite and minor gabbro, monzogranite, and syenite [58].

The Southern Terrane is interpreted as the margin of the Rae Craton, where Paleoproterozoic sedimentation occurred probably in a passive margin setting [58]. In the Southern Terrane in Prudhoe Land, Paleoproterozoic rocks overly and intrude to Neoarchean rocks of the Rae Craton [58]. The Prudhoe Land Supracrustal Complex consists of garnet-mica schist, quartzite, marble, mafic granulite, and ultramafic rocks [55]. The IMB is unconformably overlain by an unmetamorphosed cover containing the successions of two sedimentary basins (Figure 1), including (i) the sedimentary–igneous rocks of the Mesoproterozoic Thule Basin that also includes basaltic sills and (ii) the Lower Palaeozoic sedimentary rocks of the Franklinian Basin [56,62]. The Cambrian rocks of the Franklinian Basin only remained in the IMB [60,61].

The copper-gold mineralization is delimited within an NE-trending structural belt (~70 × 4 km) in the northeastern part of Inglefield Land (Figure 1). This crustal-scale structural belt consists of sulphide + graphite-bearing bands, hydrothermal alteration zones (including hematite, jarosite, biotite, chlorite, epidote, sericite assemblages, and silicification) and quartzo-feldspathic gneiss that named rust zones [1,2,63,64]. Sulfide mineralization typically comprises of pyrrhotite, pyrite, chalcopyrite, graphite, and cubanite that endured intense supergene alteration. Mylonitic or cataclastic textures were also reported locally in the rust zones. Gossans strike for several meters to up to 5 km in the mylonite and cataclasite [2,3]. Gold in several rock samples was assayed up to 12.5 ppm Au and was characteristically associated with copper (up to 4 wt%) and enriched in Zn, Mo, Ni, Co, Ba, La, and Th [2,3].

3. Materials and Methods

3.1. Satellite Remote Sensing Data and Characteristics

Landsat-8, ASTER, and WV-3 data were used in this research for mapping and detection of hydrothermal alteration minerals and lithological units associated with copper-gold mineralization

in the northeastern IMB at regional, local, and district scales. Technical characteristics of the Landsat-8, ASTER, and WV-3 sensors are shown in Table 1. Landsat-8 and ASTER data are successfully used in numerous mineral exploration projects around the world [6–12,15,16,27]. WV-3 is a high-spatial resolution commercial multispectral satellite sensor with eight VNIR (0.42 to 1.04 μm) and eight SWIR bands (1.2 to 2.33 μm), which was launched on 13 August 2014, by DigitalGlobe Incorporated from Vandenberg Air Force Base [43]. It provides high spatial resolution in panchromatic, VNIR, and SWIR with a nominal ground sample distance of 0.31 m, 1.24 m and 3.7 m, respectively (Table 1) (www.digitalglobe.com). Comparison between the spectral bands of WV-3 with Landsat-8 and ASTER emphasizes their priority and high potential for detailed mapping of alteration minerals in the VNIR and SWIR regions (Figure 2). Iron oxides/hydroxide minerals can be comprehensively mapped and discriminated by VNIR bands of WV-3 [14,19,47]. Additionally, SWIR bands of WV-3 contain excellent capability for detailed mapping of Al-OH, Mg-Fe-OH, CO3, and Si-OH key hydrothermal alteration minerals [44,45,47,49].

Table 1. Technical characteristics of the Landsat-8, Advanced Spaceborne Thermal Emission and Reflection Radiometer (ASTER), and WorldView-3 (WV-3) sensors [31,43,65].

Sensors	Subsystem	Band Number	Spectral Range (μm)	Ground Resolution (m)	Swath Width(m)
Landsat-8	VNIR	1	0.433–0.453	30	185
		2	0.450–0.515		
		3	0.525–0.600		
		4	0.630–0.680		
		5	0.845–0.885		
	SWIR	6	1.560–1.660	15	
		7	2.100–2.300		
		Pan	0.500–0.680		
	TIR	9	1.360–1.390	100	
		10	10.30–11.30		
		11	11.50–12.50		
ASTER	VNIR	1	0.520–0.600	15	60
		2	0.630–0.690		
		3	0.780–0.860		
	SWIR	4	1.600–1.700	30	
		5	2.145–2.185		
		6	2.185–2.225		
		7	2.235–2.285		
		8	2.295–2.365		
		9	2.360–2430		
	TIR	10	8.125–8.475	90	
		11	8.475–8.825		
		12	8.925–9.275		
		13	10.25–10.95		
		14	10.95–11.65		
WV3	VNIR	Costal (1)	0.400–0.450	1.24	13.1
		Blue (2)	0.450–0.510		
		Green (3)	0.510–0.580		
		Yellow (4)	0.585–0.625		
		Red (5)	0.630–0.690		
		Red edge (6)	0.705–0.745		
		Near-IR1 (7)	0.770–0.895		
		Near-IR2 (8)	0.860–1.040		

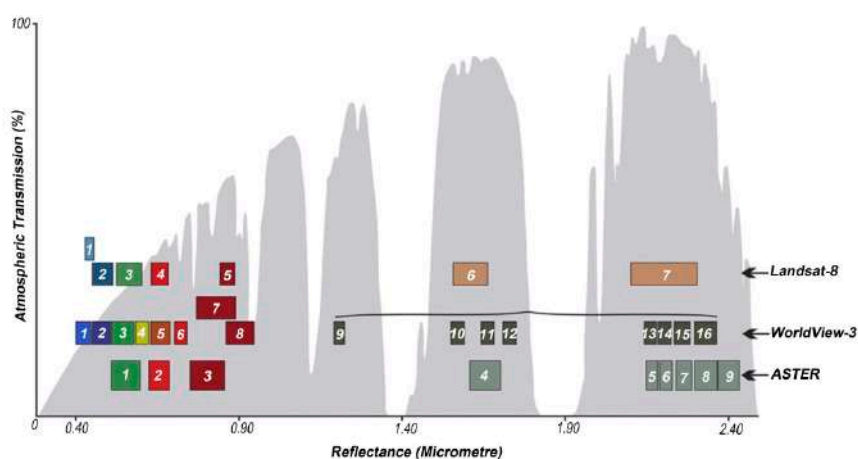|	SWIR-1 (9)	1.195–1.225	
	SWIR-1 (10)	1.550–1590	
	SWIR-1 (11)	1.640–1.680	
SWIR	SWIR-1 (12)	1.710–1.750	3.70
	SWIR-1 (13)	2.145–2.185	
	SWIR-1 (14)	2.185–2.225	
	SWIR-1 (15)	2.235–2.285	
	SWIR-1 (16)	2.295–2.365	

Figure 2. Comparison of the spectral bands of WV-3 with Landsat-8 and ASTER in the visible and near-infrared (VNIR) and shortwave infrared (SWIR) regions [46].

In this study, two Landsat-8 scenes (LC80350032018233LGN00 and LC80350042018233LGN00) covering Inglefield Land were acquired from the U.S. Geological Survey Earth Resources Observation and Science Center (EROS) (https://earthexplorer.usgs.gov/). The data set attributes of these images are summarized as follows: acquisition date: 21 August 2018, collection category: T1 (terrain corrected), Path/Raw: 035/003 and 035/004, scene cloud cover: 11.97% and 2.18%, sun elevation: 22.115 and 23.400 and sun azimuth: −158.241 and −163.695. An ASTER scene (AST_L1T_003070022003234340) covering the northeastern IMB was obtained from the EROS, USGS Global Visualization Viewer (GloVis) (https://glovis.usgs.gov/). It is a level 1T product which is cloud-free and it was acquired on 3 July 2003. The ASTER Level 1 Precision Terrain Corrected Registered At-Sensor Radiance (AST_L1T) data contains calibrated at-sensor radiance, which corresponds with the ASTER Level 1B (AST_L1B), that has been geometrically corrected, and rotated to a north up UTM projection (https://lpdaac.usgs.gov). Some WV-3 scenes were obtained by courtesy of the DigitalGlobe Foundation (www.digitalglobefoundation.org). The VNIR imagery (M2AS-059185278010_01_P001) of the northeastern IMB was granted by the DigitalGlobe Foundation (Copyright 2019 DigitalGlobe, Inc., Longmont CO USA 80503-6493), which was cloud-free, standard level 2 A and acquired on 25 August 2018. The Level 2A standard WV-3 imagery product contains a uniform Ground Sample Distance (GSD), which is radiometrically corrected, sensor corrected, and geometrically projected to the Universal Transverse Mercator (UTM) with the World Geodetic System 84 (WGS-84) datum [66,67]. The Environment for Visualizing Images (ENVI) (http://www.exelisvis.com) version 5.2 and ArcGIS version 10.3 (Esri, Redlands, CA, USA) software packages were utilized for processing Landsat-8, ASTER, and WV-3 datasets.

3.2. Pre-Processing of the Datasets

The Landsat-8 images were pre-georeferenced to the UTM zone 19 and 20 North projection using the WGS84 datum. The ASTER and WV-3 images were also pre-georeferenced to UTM zone 19 North projection using the WGS-84 datum. Atmospheric correction is required to eradicate the impact of

atmospheric attenuation from remote sensing imagery and to re-scale the radiance at the sensor data to the surface reflectance data. The absolute radiometric correction and conversion to the top-of-atmosphere (TOA) spectral radiance are required for the WV-3 relative radiometrically corrected images [66]. Hence, these corrections were applied to WV-3 VNIR data used in this study. Crosstalk correction [68] was applied to ASTER data and layer staked of VNIR + SWIR bands with 15-meter spatial dimensions was generated. The Fast Line-of-sight Atmospheric Analysis of Hypercubes (FLAASH) algorithm [69] were applied to the remote sensing datasets used in this research by implementing the sub-arctic summer (SAS) atmospheric and the Maritime aerosol models [70]. ASTER TIR (radiance at the sensor) data without atmospheric corrections were used in this analysis for retaining the original radiance signature.

3.3. Image Processing Algorithms

### 3.3.1. Directed Principal Components Analysis (DPCA) Technique

The DPCA is a direct information extraction technique to analyze the principal component (PC) eigenvector loadings for selecting the most appropriate PC that focuses the most noteworthy information of interest [71–73]. The magnitude and sign of eigenvector loadings specify whether interesting information is characterized by a bright (positive loading) or a dark pixel (negative loading) in the DPCA image [74]. To map hydrothermal alteration mineral assemblages, including (i) hematite and jarosite (iron oxide/hydroxide group), (ii) biotite and sericite (Al/Fe-OH group), (iii) chlorite and epidote (Mg-Fe-OH group), and (iv) silicification (Si-OH group (opal/chalcedony) and/or SiO2 group) in the study area, some specialized band ratios were defined to be used as input datasets for running the DPCA. The variance due to similarities in the spectral responses of the interfering component and the component of interest appear in eigenvector loadings of similar signs on input band ratio images. The DPCA contains strong eigenvector loadings of different signs on the input band ratio images, showing a specific contribution of the component [73,74].

For mapping hydrothermal alteration minerals associated with rust zones in the copper-gold mineralization belt, spectral characteristics of hematite, jarosite, biotite, muscovite, chlorite, epidote, chalcedony (hydrous-silica), and opal (hyalite) were considered to identify using the DPCA technique. Figure 3A–C shows laboratory reflectance spectra of hematite, jarosite, biotite, muscovite, chlorite, epidote, chalcedony (hydrous-silica), and opal (hyalite) resampled to response functions of VNIR + SWIR bands of Landsat-8, ASTER, and WV-3, that were extracted from the USGS spectral library version 7.0 [75]. For mapping the alteration mineral groups using Landsat-8 spectral bands, several band ratio indices were adopted and developed [7,8,76]. Band ratio indices of 4/2 (all iron oxides), 6/4 (ferrous iron oxides), 6/5 (ferric oxides), and 6/7 (hydroxyl bearing alteration) can be allotted as significant indicators of Fe^{3+}, Fe^{2+}, Al/Fe-OH, Mg-Fe-OH, and Si-OH groups using Landsat-8 spectral bands (see Figure 3A). Additionally, the normalized difference snow index (NDSI), Al-OH-bearing alteration minerals index (Al-OH-MI) and thermal radiance lithology index (TRLI) were used for mapping snow/ice, cloud, water, alteration OH minerals, and land and lithologies [7]. For mapping iron oxide/hydroxide mineral groups using Landsat-8 bands, three band ratios were developed on the basis of the laboratory spectra of the minerals [77,78]. Hematite, jarosite, goethite, and limonite tend to have strong absorption features in 0.4 to 1.1 μm (absorption features of Fe^{3+} near 0.45 to 0.90 μm and Fe^{2+} near 0.90 to 1.2 μm) [77,78] coincident with bands 2, 4, and 5 and high reflectance at 1.56 μm to 1.70 μm equivalent with band 6 (Figure 3A). As a result, bands 2, 4, 5, and 6 of Landsat-8 can be used for detecting Fe^{3+}/Fe^{2+} and Fe-OH iron oxides (4/2), ferrous iron oxides (6/4), and ferric oxides (6/5). Hydroxyl-bearing (Al-OH and Fe, Mg-OH) alteration has spectral absorption features in 2.1–2.4 μm and reflectance in 1.55–1.75 μm [35], corresponding band 7 (2.11–2.29 μm) and band 6 (1.57–1.65 μm) of Landsat-8 (Figure 3A), respectively. Therefore, band ratio of 6/7 can map hydroxyl bearing alteration. The DPCA was applied to the Landsat-8 band ratio indices (4/2, 6/4, 6/5, and 6/7) using a covariance matrix for obtaining the image eigenvectors and eigenvalues.

(A)   **(Landsat-8)**
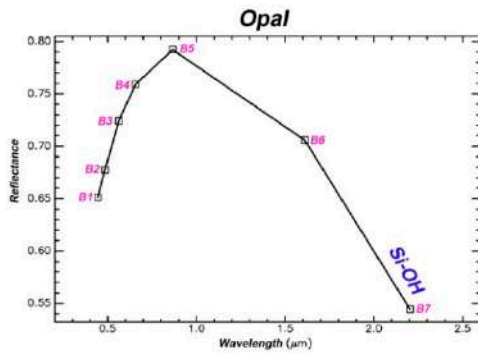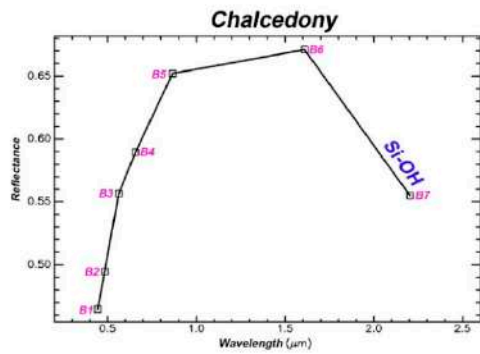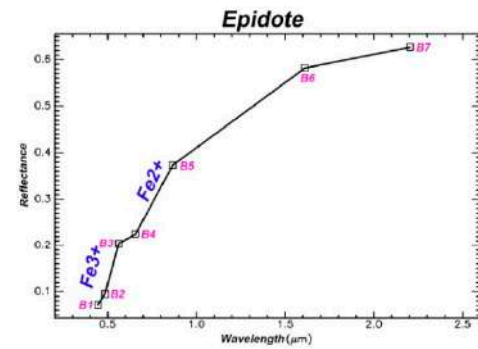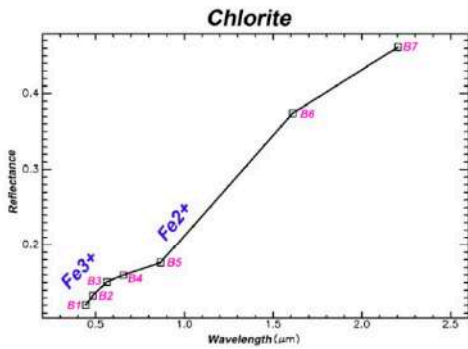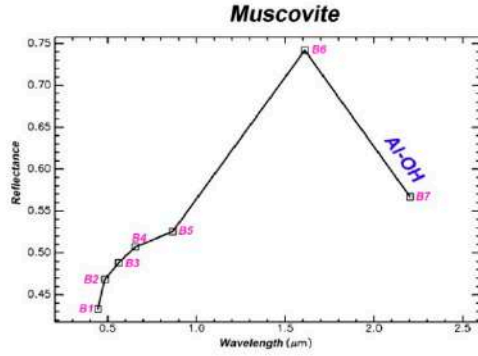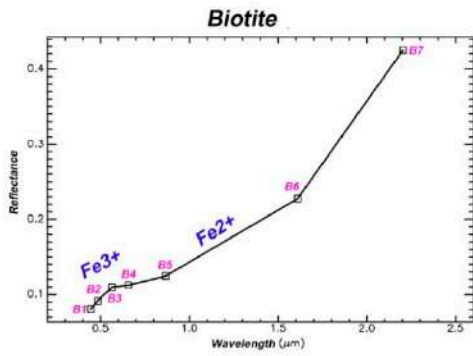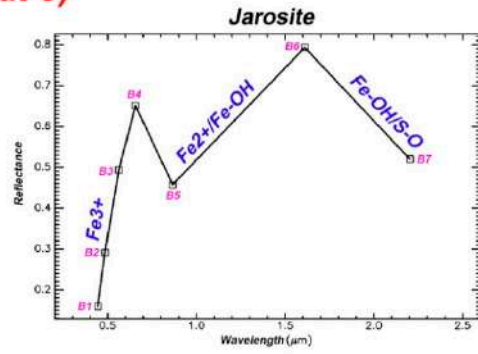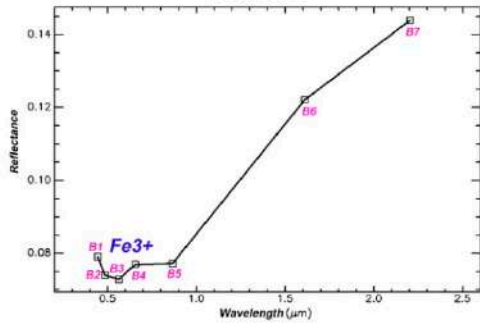
(B)
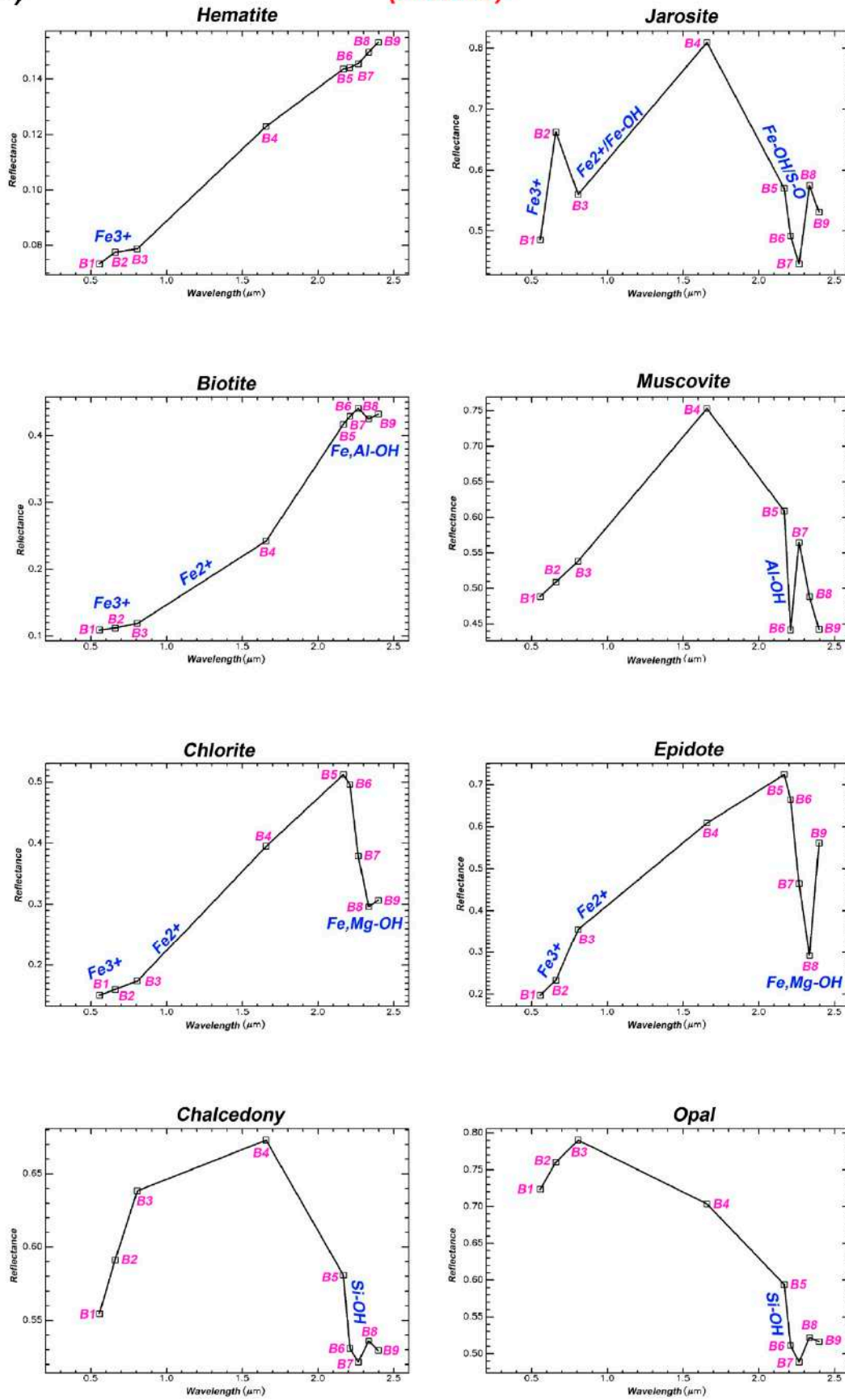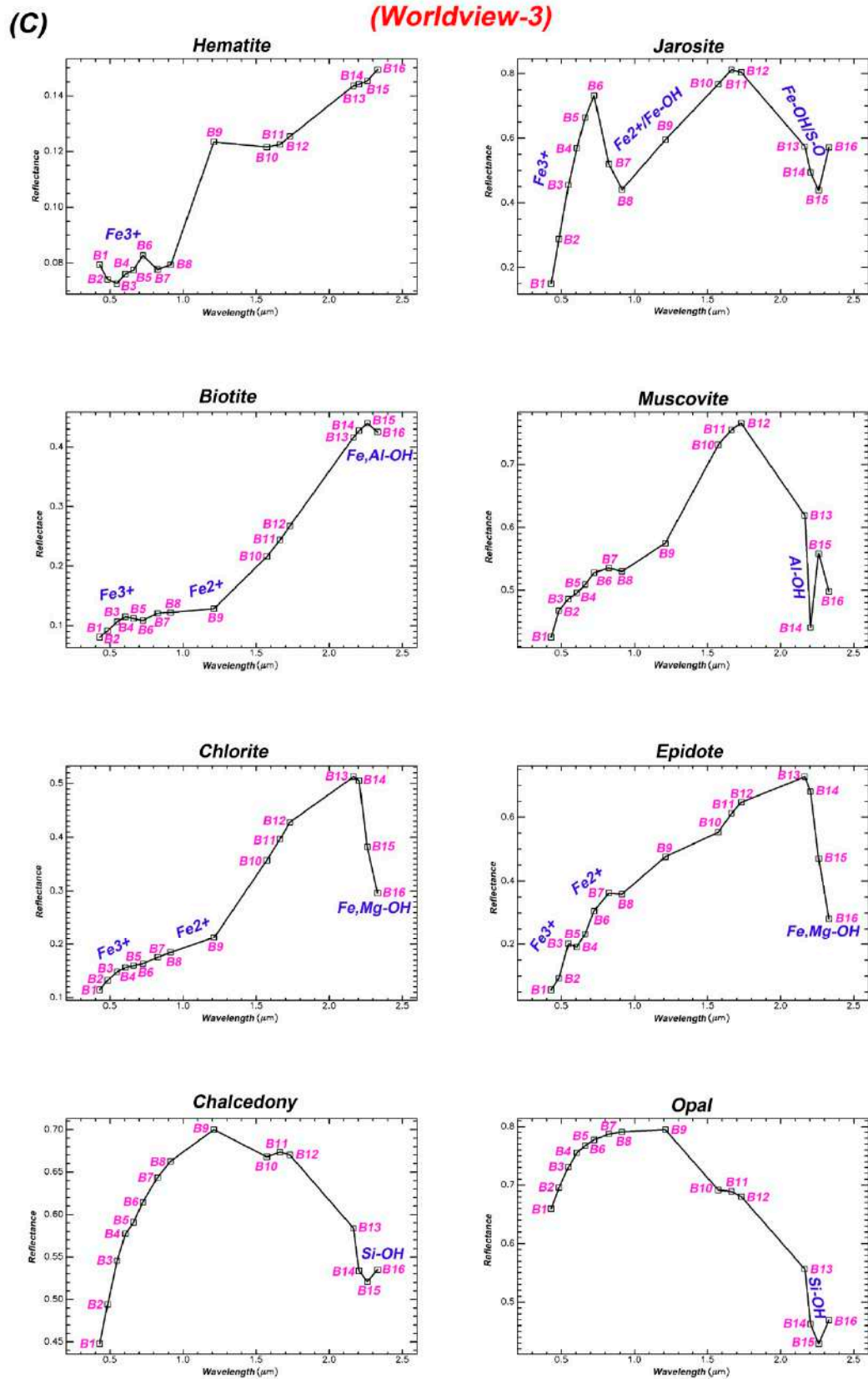
(ASTER)

Figure 3. Laboratory reflectance spectra of hematite, jarosite, biotite, muscovite, chlorite, epidote, chalcedony (hydrous-silica), and opal (hyalite) resampled to response functions of VINR + SWIR bands of Landsat-8 (**A**), ASTER (**B**), and WV-3 (**C**) that were extracted from the USGS spectral library version 7.0 [75]. Cubes indicate the position of the VINR + SWIR bands of Landsat-8, ASTER, and WV-3 in the range of 0.4 μm to 2.5 μm.

Several band ratio indices were tested for mapping the alteration mineral groups using ASTER spectral bands (see Figure 3B). The band ratios of 2/1 and 4/2 were selected to map Fe^{3+}/Fe^{2+} iron oxides; (5 + 7)/6 was adopted to detect Al/Fe-OH minerals; (7 + 9)/8 was assigned to identify Mg-Fe-OH minerals [79]; and (6 + 8)/7 were developed to map Si-OH minerals, respectively. Bands 1 (0.520–0.600 µm), 2 (0.630–0.690 µm) and 4 (1.600–1.700 µm) of ASTER cover the spectral absorption and reflectance features of iron oxide/hydroxide minerals. Thus, band ratios of 2/1 and 4/2 can be utilized for detecting Fe^{3+}/Fe^{2+} iron oxides. Al-OH absorption features at 2.17 to 2.20 µm [35,77,78] are corresponded with bands 5 and 6, whereas Mg-Fe-OH absorption features are situated in 2.30 to 2.35 µm [35,77,78] that are equivalent with bands 7 and 8 of ASTER (Figure 3B). Si-OH absorption features are mostly concentrated at 2.20 to 2.30 µm, which are coincident with bands 6 and 7 of ASTER (Figure 3B). Subsequently, relative absorption band depth (RBD) [80] of these bands can be used to map Al/Fe-OH ((5 + 7)/6), Mg-Fe-OH ((7 + 9)/8), and Si-OH ((6 + 8)/7) minerals. The DPCA was implemented to the band ratio indices (2/1, 4/2, (5 + 7)/6 and (7 + 9)/8) using a covariance matrix for the spatial selected subset covering the Cu-Au mineralization belt and surrounding areas. Furthermore, for mapping silica-rich rocks containing SiO_2 group, Quartz Index (QI) = 11 × 11/10 × 12, Carbonate Index (CI) = 13/14, and Mafic Index (MI) = 12/13 were selected [81] and applied to TIR bands of ASTER. These lithologic indices were defined by Ninomiya et al. [81] for discriminating quartz, carbonate, and mafic-ultramafic rocks, especially for mapping lithological units in arid and semi-arid regions. The DPCA was employed to these indices. Eigenvector matrix was calculated using a covariance matrix for the spatial selected subset covering the Cu-Au mineralization belt and surrounding areas.

The VNIR spectral bands of WV-3 contain the high capability to map Fe^{3+} and Fe^{2+} iron oxides (gossan), ferric, and ferrous silicates. Considering the laboratory reflectance spectra of selected minerals (see Figure 3C), the band ratio indices of 4 + 2/3 to map Fe^{3+} iron oxides, 6 + 8/7 for identifying Fe^{2+} iron oxides, 3 + 5/4 to detect ferric silicates (chlorite/epidote), and 5 + 7/6 for enhancing ferrous silicates (biotite) were developed. These indices were used to implement the DPCA using a covariance matrix for the spatial selected subset covering the southern part of the Cu-Au mineralization belt. The DPCA statistical results were also calculated for the WV-3 band ratio indices.

3.3.2. Linear Spectral Unmixing (LSU)

The LSU is a sub-pixel image processing algorithm, which is utilized to define the relative abundance of materials that can be diagnosed within optical imagery based on the materials' spectral properties [82–84]. The reflectance at each pixel of the image is presumed to be a linear combination of the reflectance of each material (or end-member) existing within the pixel. It is advocated in this algorithm that the pixel reflectance could be shown as a linear mixture of individual component reflectance multiplied by its relative fractions [85]. For extracting reference spectra directly from the Landsat-8, ASTER, and WV-3 images to generate fraction images of end-members using the LSU, the automated spectral hourglass (ASH) approach was implemented [86,87]. This approach contains the minimum noise fraction (MNF), the pixel purity index (PPI) and automatic end-member prediction from the n-Dimensional Visualizer to extract the most spectrally pure pixels (end-members) from the image [88,89]. Additionally, the continuum-removal process was performed to the extracted end-members for isolating their spectral features [90]. Then, the end-members were compared with the USGS library reflectance spectra of target minerals, including hematite, jarosite, biotite, muscovite, chlorite, epidote, chalcedony (hydrous-silica), and opal (hyalite) (see Figure 3A–C). Umix unit-sum constrained was adjusted 1.0 for running the LSU algorithm. This weighted unit-sum constraint is then added to the system of simultaneous equations in the unmixing inversion process. Larger weights in relation to the variance of the data cause the unmixing to honor the unit-sum constraint more closely. To strictly honor the constraint, the weight should be many times the spectral variance of the data. It also permits proper unmixing of MNF transform data, with zero-mean bands [70]. For interactive stretching histogram, auto apply option was selected to have stretching or histogram changes applied to the images automatically. Rule image classifier tool was used for post

classification of the LSU rules images. Maximum value option was selected. Threshold value for classification of fraction images derived from the LSU algorithm was 0.750.

3.3.3. Adaptive Coherence Estimator (ACE)

The ACE is a target detection algorithm that carries out a partial unmixing approach to isolate feature of interest from the background and its input is a single score (abundance of the target) per pixel [91]. It is generated from the generalized likelihood ratio (GLR) approach, which is a homogenously most powerful invariant detection statistic [92,93]. The ACE is invariant to the relative scaling of input spectra and has a constant false alarm rate (CFAR) for such scaling [94]. Geometrically, it determines the squared cosine of the angle between a known target vector and a sample vector in a whitened coordinate space. The space is faded based on assessing the background statistics, which straightforwardly influences the presentation of the statistic as a target detector [95]. The standard formulation of the ACE detection statistic is defined as follows:

$$ACE(x) = \frac{[(t-\mu)^T \Sigma^{-1}(x-\mu)]^2}{[(t-\mu)^T \Sigma^{-1}(t-\mu)][(x-\mu)^T \Sigma^{-1}(x-\mu)]} \tag{1}$$

where t is a known target signature (reference spectra from a spectral library signature) and x is a data sample. The background is assumed to be a Gaussian distribution parametrized by u and Σ which represent the mean and covariance, respectively. The ACE statistic is a number between zero and one, which can be interpreted as a measurement of the presence of t in x. The ACE can be estimated as the square of the cosine of the angle between x and t, in a coordinate space transformed by the background estimation. For example, if ACE produces 0.85, indicating a relatively strong presence of t in x. The key to effective ACE performance is accurate background estimation. Furthermore, the ACE does not need information about all the end-members within an image scene. In this study, the ACE algorithm was applied to VNIR + SWIR bands of ASTER covering the Cu-Au mineralization belt and surrounding areas. Laboratory reflectance spectra of hematite, jarosite, biotite, muscovite, chlorite, epidote, chalcedony (hydrous-silica), and opal (hyalite) extracted from USGS spectral library version 7.0 [75] were used for running the ACE algorithm. New covariance statistics were computed and subspace background was used. Background threshold was adjusted 0.900. The results of ACE appear as a series of grayscale images, one for each selected end-member.

4. Results

4.1. Regional Lithological-Mineralogical Mapping in Inglefield Land Using Lansat-8 Data

A regional view of the northwestern part of Greenland was generated using a mosaic of Landsat-8 images (Figure 4). The NDSI, Al-OH-MI, and TRLI [7] were used for mapping snow/ice, cloud, water, land, and lithologies. The NDSI (B3 − B6/B3 + B6), Al-OH-MI (B6/B7) × (B7), and TRLI (B10/B11) × (B11) were assigned to Red-Green-Blue false-color composite, respectively (Figure 4). The ice/snow zones appear in magenta, red, and orange shades that correspond to the different snow/ice facies. Stratocumulus cloud coverage is represented as golden yellow especially in the east and northeastern parts (inland ice) of the mosaic image-map. Water is depicted in a dark blue color. The Inglefield Land and Washington Land in the west and northwestern parts of the scene appear in light blue and cyan shades. The shelf-platform carbonate of the Franklinian Basin in the Washington Land and northwestern parts of the Inglefield Land (adjacent to Smith Sound) typically contains cyan shade. The exposed lithologies, including the complex metamorphic rocks of the Central Terrane and the Southern Terrane and Mesoproterozoic sedimentary–igneous rocks of the Thule Basin manifest in a light blue tone (Figure 4).
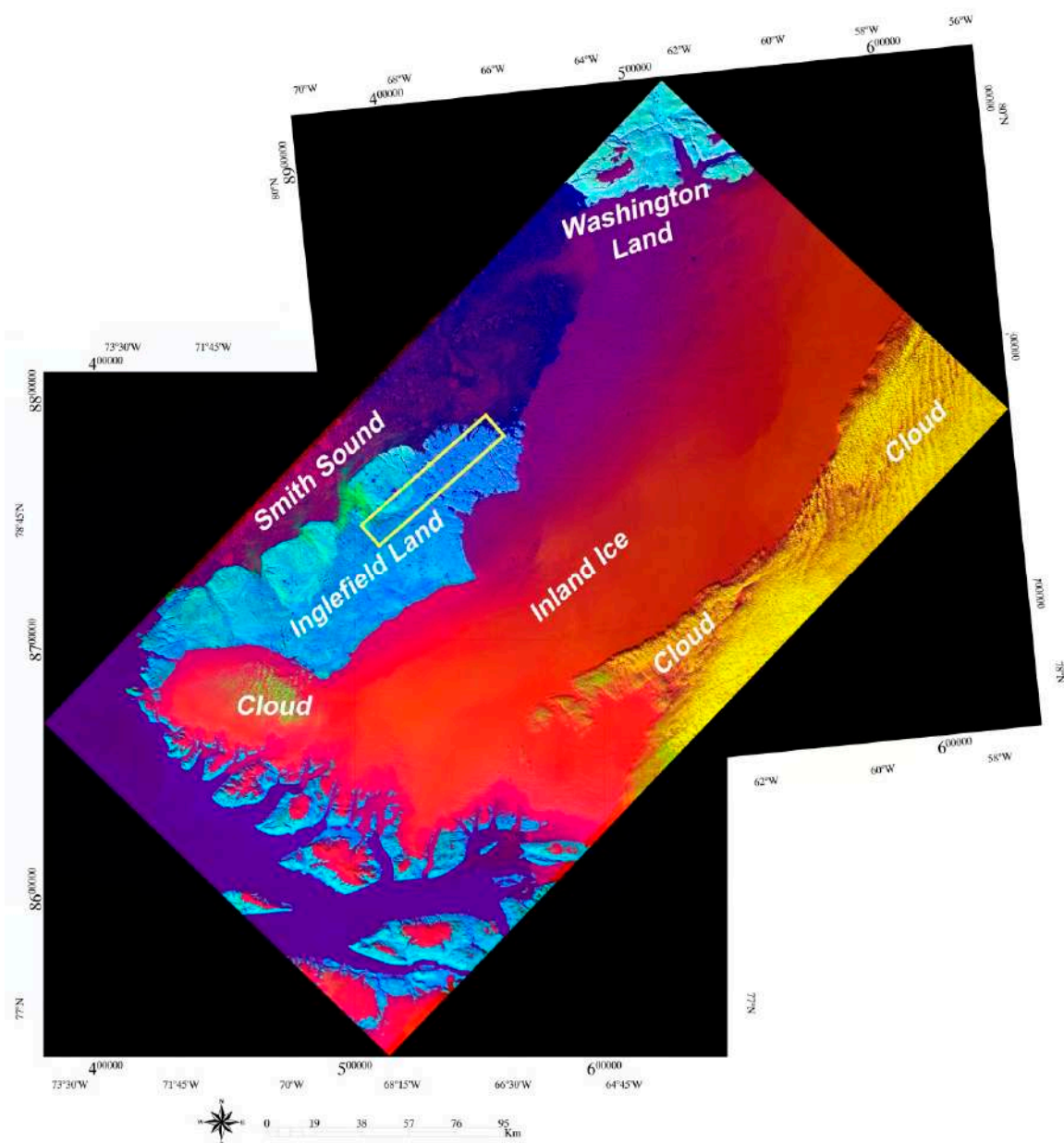
Figure 4. A regional view of the northwestern part of Greenland generated using a mosaic of Landsat-8 images as RGB false-color composite of the normalized difference snow index (NDSI), Al-OH-bearing alteration minerals index (Al-OH-MI), and thermal radiance lithology index (TRLI). Yellow rectangle shows the location of the Cu-Au mineralization belt.

Band ratio indices of B4/B2, B4/B6, and B6/B7 were assigned to the RGB false-color composite for mapping iron oxides/hydroxides, ferrous iron oxides, and hydroxyl bearing alteration zones in the IMB at the regional scale, respectively. Figure 5A shows the resultant image-map. Regarding the geology map of the IMB (see Figure 1), the sedimentary successions of the Franklinian Basin and Thule Supergroup appear typically in cyan, pink, orange, and rose blush. Carbonate and siliciclastic rocks are dominant lithological units in these two sedimentary basins, which are mostly represented as cyan color. It could be due to the fact that most of Al-OH, Mg-Fe-OH, CO3, and Si-OH mineral groups show high reflectance at 1.55–1.75 μm and strong absorption at 2.1–2.4 μm coincident with bands 6 and 7 of Landsat-8, respectively [7,76]. Pink, orange, and rose blush zones may contain dolomite (Fe^{2+} absorption at 0.9–1.2 μm; the equivalent of band 5 of Landsat-8) or iron oxides/hydroxides minerals. Basaltic sills in the Thule Basin are depicted in purple color (western

part of image-map) due to the high content of iron oxides/hydroxides minerals. Several golden yellow areas are recognizable at the boundaries between sedimentary successions and the Etah metamorphic complex rocks in the Central Terrane, which comprise Fe^{3+} and Fe^{2+} iron oxides/hydroxides. Paragneiss of the Etah Group manifests in magenta to tangerine tone in both the Southern and Central Terranes due to a strong amount of iron oxides/hydroxides, while Quaternary deposits appear as cyan color because of detrital clay minerals. Syenite of the Etah meta-igneous complex is characterized by brown color adjacent to the Sunrise Pynt Shear Zone. Orthogneiss in the western and northeastern parts of the IMB shows up in gray shade (Figure 5A). Syenite and orthogneiss probably contain a high amount of ferrous iron oxide minerals attributable to alteration products of primary mafic minerals such as biotite, hornblende, amphibole, and clinopyroxene (augite).
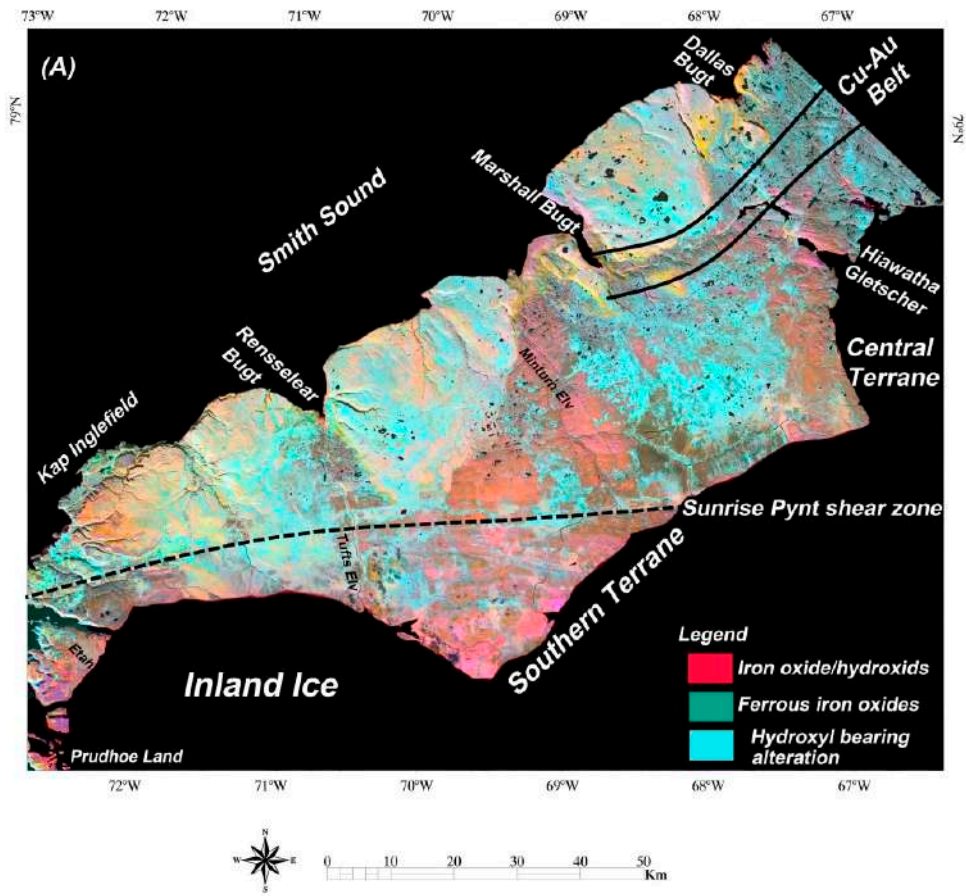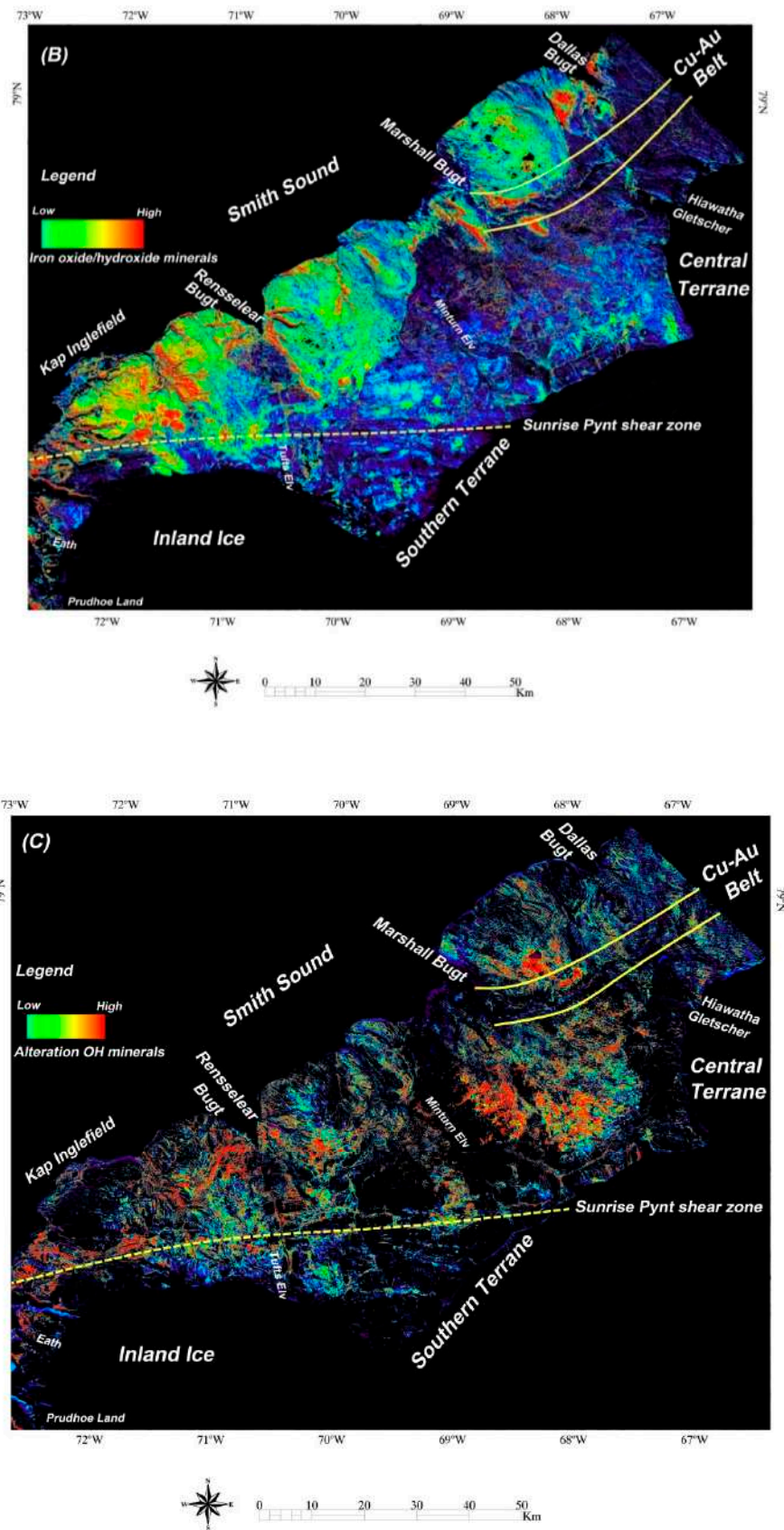
Figure 5. Landsat-8 image-maps of the IMB. (**A**) RGB false-color composite of B4/B2, B4/B6, and B6/B7 band ratio indices covering the IMB. (**B**) Pseudocolor ramp of the DPCA3 rule image covering the IMB. (**C**) Pseudocolor ramp of the DPCA4 rule image covering the IMB.

Table 2 shows the eigenvector matrix of the Landsat-8 band ratio indices (4/2, 4/6, 6/5, and 6/7) derived from the DPCA for the selected subset covering the IMB. Analyzing the magnitude and sign of the eigenvector loadings derived from DPCA technique for the IMB selected subset scene (Table 2) indicates the DPCA1 contains positive eigenvector loadings for all input band ratio indices. Thus, it does not have any unique contribution of input band ratio indices and the discrimination of alteration mineral groups is impossible. The DPCA2 has a strong negative contribution (−0.770751) for ferric oxides (B6/B5). However, it contains moderate loadings of other alteration mineral groups with the opposite sign (Table 2). Ferric oxides manifest as dark pixel in the DPCA2 image due to negative loading. The DPCA3 contains strong positive loadings of B4/B2 (0.686248) and B4/B6 (0.714648) for iron oxides/hydroxides and ferrous iron oxides mineral groups, respectively (Table 2). However, the eigenvector loadings in the DPCA3 for ferric oxides (B6/B5) and hydroxyl bearing alteration (B6/B7) indices are weak and negative (−0.124892 and −0.052382). Therefore, the DPCA3 image shows desired information related to Fe^{3+} and Fe^{2+} iron oxides/hydroxides as bright pixel. Figure 5B shows a pseudocolor ramp of the DPCA3 rule image. The high concentration of Fe^{3+}/Fe^{2+} iron oxides/hydroxide minerals is observable in the boundaries between the Etah metamorphic complex rocks and sedimentary successions of the Franklinian Basin and Thule Supergroup in the Central Terrane. Moderate to low abundance of iron oxides/hydroxide minerals are associated with carbonate and siliciclastic rocks in both sedimentary basins. The southern part of the Cu-Au mineralization belt nearby Marshall Bugt contains high surface abundance of iron oxides/hydroxide minerals. The Etah group and meta-igneous complex rocks show moderate to low spatial distribution of iron oxides/hydroxide minerals. Some of the highly abundant iron oxides/hydroxide zones are located in Quaternary deposits and associated with Basaltic sills in the Thule Basin (Figure 5B).

Table 2. Eigenvector matrix of the Landsat-8 band ratio indices derived from the directed principal components analysis (DPCA) for the Inglefield Mobile Belt (IMB) selected subset scene.

Eigenvector	B4/B2	B6/B4	B6/B5	B6/B7
DPCA 1	0.412529	0.470934	0.624086	0.467501
DPCA 2	0.459849	0.282028	−0.770751	0.339030
DPCA 3	0.686248	0.714648	−0.124892	−0.052382
DPCA 4	-0.383955	-0.433543	−0.029349	0.814713

The Al-OH, Mg-Fe-OH, CO3 and Si-OH alteration mineral groups are mapped in the DPCA4 image due to the great positive contribution of B6/B7 ratio index (0.814713) (Table 2). On the other hand, iron oxides/hydroxides (−0.383955), ferrous iron oxides (−0.433543), and ferric oxides (−0.029349) indices show moderate to weak eigenvector loadings with a negative sign in the DPCA4 (Table 2). It is evident that the DPCA4 image shows the alteration OH mineral groups as bright pixels. A pseudocolor ramp of the DPCA4 rule image was generated (Figure 5C). High spatial distribution of the alteration OH mineral groups is mostly associated with carbonate and siliciclastic units of the Franklinian Basin and Thule Supergroup as well as Quaternary deposits in the Central Terrane. Moreover, orthogneiss of the Etah meta-igneous complex and marble, amphibolite, and calc-silicate rocks of the Etah group show a high surface abundance of alteration OH mineral groups. The central part of the Cu-Au mineralization belt contains a remarkable concentration of the alteration OH mineral groups, which might be related to amphibolite or alteration products of quartz diorite units. Paragneiss of the Etah Group includes low to moderate surface distribution of the alteration OH minerals.

Figure 6A displays end-member spectra (n-D classes) extracted from the n-Dimensional analysis technique for a selected spatial subset of Landsat-8 covering the Cu-Au mineralization belt and surrounding areas. The n-D classes correspond to a set of unique pixels (a pure end-member), which are used to act as end-members for the LSU spectral mineral-mapping. Comparison of the extracted n-D classes with selected end-member reflectance spectra of the target minerals from the USGS spectral library (see Figure 3A) indicates that some of the n-D classes could be considered for the LSU spectral mineral-mapping. Some noticeable similarities between spectral signatures of the n-D classes

and the target minerals could be utilized for identifying iron oxide/hydroxide, clay mineral groups and ferrous silicates (biotite, chlorite and epidote). The n-D class #1 and n-D class #6 typically represent Al-OH/Si-OH absorption characteristics (Figure 6A). Muscovite, chalcedony, and opal show high reflectance in band 6 (1.560–1.660 μm) and strong absorption in band 7 (2.100–2.300 μm) of Landsat-8 (see Figure 3A). The n-D class #2 and n-D class #4 can be considered as snow/ice/cloud group because these classes show high reflectance in the visible wavelengths from 0.40 μm to 0.75 μm (band 1 to band 4 of Landsat-8), lower reflectance in the near-infrared from 0.80 μm to 0.90 μm (band 5 of Landsat-8), and strong absorption in the short wave infrared from 1.57 μm to 1.78 μm (band 6 of Landsat-8) [96–98]. The n-D class #3 does not show any typical absorption features related to any geological materials and hydrothermal alteration minerals. The n-D class #5 contains some similar spectral signatures related to Mg-Fe-OH alteration minerals (ferrous silicates). Iron oxide (Fe^{+2}/Fe^{+3}) absorption features in bands 2 to 3 (0.50–0.60 μm) and bands 4 to 5 (0.70–0.90 μm) and Mg, Fe-OH absorption in bands 7 of Landsat-8 are recognizable for the n-D class #5 (Figure 6A). The n-D class #7 and n-D class #8 might be attributed to the iron oxide/hydroxide minerals because of Fe^{3+} and Fe-OH absorption features at 0.45 μm to 0.70 μm, 0.80-0.90 μm, and 2.20-2.30 μm coinciding with bands 2, 3, 4, 5, and 7 of Landsat-8.
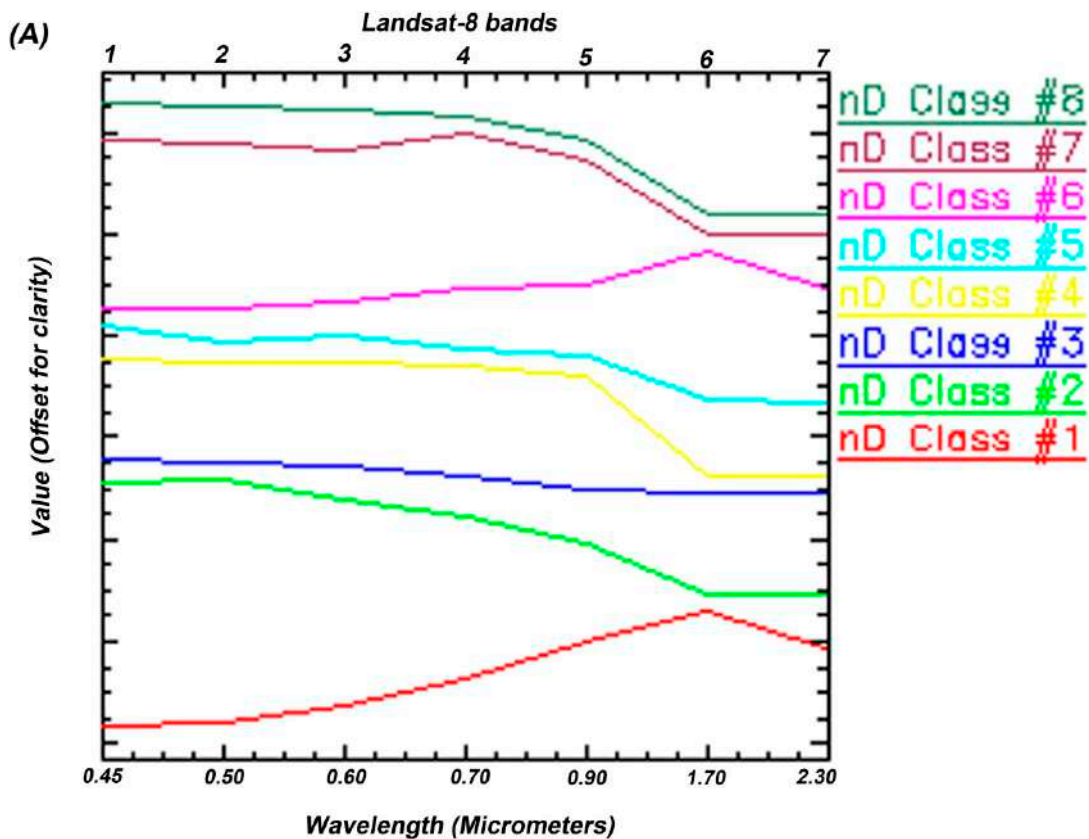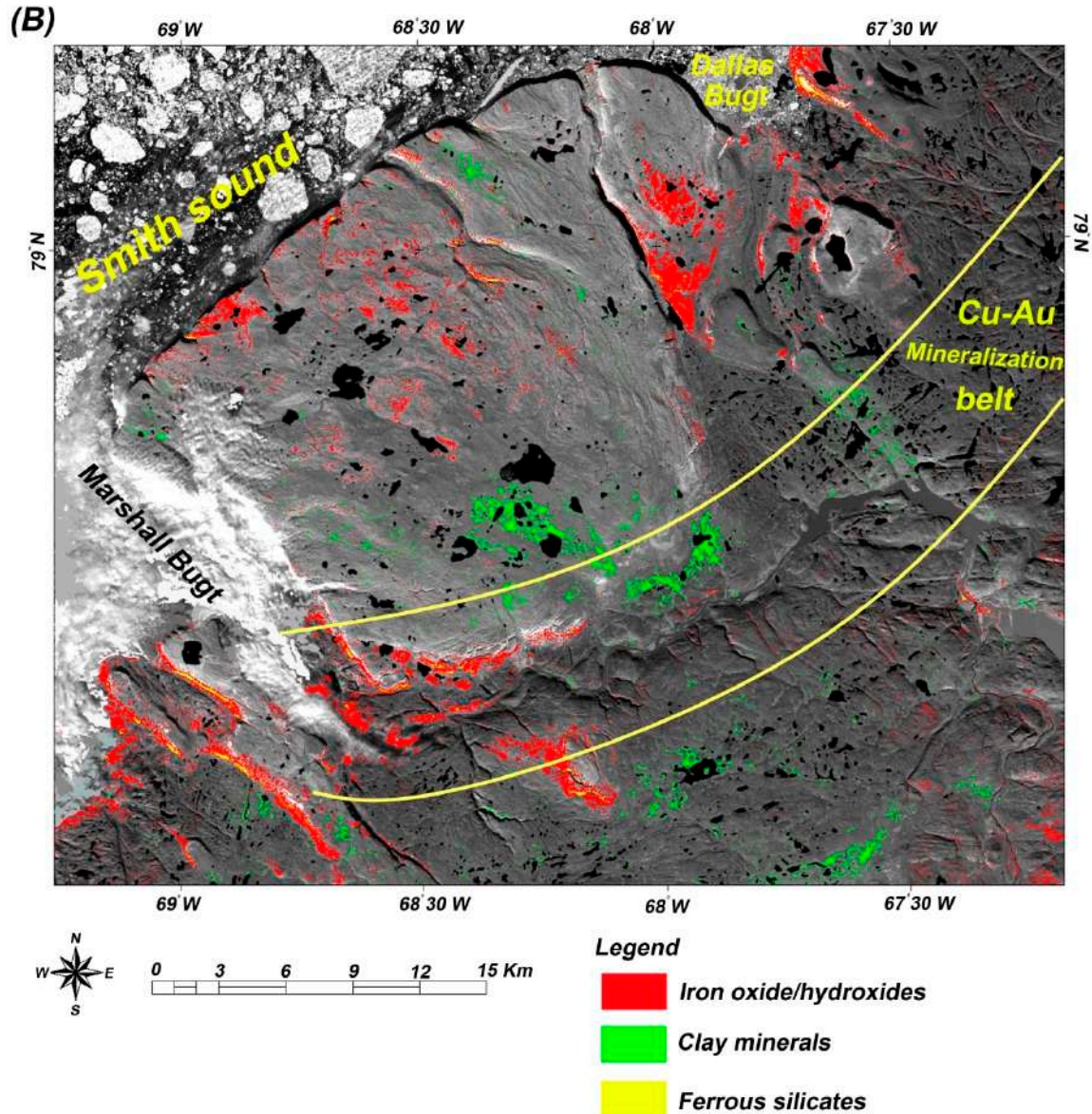
Figure 6. (A) The n-D classes (end-member spectra) extracted for a selected spatial subset (Landsat-8) covering Cu-Au mineralization belt and surrounding areas. Landsat-8 band center positions are shown. **(B)** LSU mineral map produced from fraction images overlaid on band 5 of Landsat-8 for the selected spatial subset covering the Cu-Au mineralization belt and surrounding areas.

Fraction images of the end-members resulted from the LSU algorithm manifest as a series of greyscale rule images (one for each extracted end-member). Considering the resultant fraction images and the n-D classes (extracted end-member spectra) for the Landsat-8 selected subset, it is evident that iron oxide/hydroxide minerals, clay minerals and ferrous silicates are main alteration mineral groups in the study area. For post-classification of the fraction images (excluding snow/ice/cloud group) the interactive density slicing tool was used to select colors for highlighting the high digital number (DN) value areas (bright pixels) in the grayscale rule images. The red color class was considered for iron oxide/hydroxide group, the green color class was selected for clay mineral groups, and the yellow color class was assigned for ferrous silicates, respectively. Figure 6B shows the LSU spectral mineral-map for the Landsat-8 selected subset covering the Cu-Au mineralization belt and surrounding areas. Iron oxide/hydroxide minerals (red pixels) are spectrally dominated in the image-map, whereas clay minerals and ferrous silicates show less spatial distribution in the selected subset. Comparison to the geological map of the study zone, suggests that an iron oxide/hydroxide group is

typically concentrated in the southwestern part of the Cu-Au mineralization belt at the boundary between orthogneiss and paragneiss with the sedimentary succession of carbonate and basal siliciclastic rocks. However, an iron oxide/hydroxide group is also detected in the Franklinian Basin sedimentary succession (central north) and many other zones in orthogneiss and paragneiss of the Etah complex in the southwestern and southeastern parts of the scene (Figure 6B). The high surface abundance of clay minerals (green pixels) was mapped in orthogneiss, amphibolite, and quartz diorite units especially in the central part of the Cu-Au mineralization belt. Basal siliciclastic rocks of the Franklinian Basin show high concentrations of clay minerals in the central part of the scene. Ferrous silicates are lesser in the surface abundance and generally associated with an iron oxide/hydroxide mineral group (Figure 6B).

4.2. Hydrothermal Alteration Mapping in the Northeastern IMB Using ASTER Data

Analyzing the eigenvector matrix of the band ratio indices for mapping hydrothermal alteration minerals using VNIR + SWIR bands of ASTER (Table 3) shows that the DPCA technique detected the surface distribution of Fe^{3+}/Fe^{2+} iron oxide/hydroxides, Al/Fe-OH, Mg-Fe-OH, and Si-OH minerals in some specific DPCA images with a strong contribution of the input band ratio components. Figure 7A–E shows the pseudocolor ramp of the DPCA rule images covering the selected spatial subset of the Cu-Au mineralization belt and surrounding areas (similar size as the Landsat-8 LSU image-map).

Table 3. Eigenvector matrix of the ASTER VNIR + SWIR band ratio indices derived from the DPCA for the selected subset covering the Cu-Au mineralization belt and surrounding areas.

Eigenvector	B2/B1	B4/B2	B5 + B7/B6	B7 + B9/B8	B6 + B8/B7
DPCA 1	−0.219557	−0.347765	−0.900627	−0.123124	−0.067567
DPCA 2	−0.547623	0.589087	−0.177962	−0.235635	−0.434915
DPCA 3	0.263209	0.141891	−0.759215	0.418035	0.399283
DPCA 4	−0.027870	−0.119071	0.531229	0.709489	−0.288482
DPCA 5	−0.568874	0.044535	0.108190	0.314737	−0.750756

The DPCA2 contains a strong contribution of Fe^{3+}/Fe^{2+} iron oxide/hydroxides in the B2/B1 (−0.547623) and B4/B2 (0.589087), while the contributions of Al/Fe-OH, Mg-Fe-OH, Si-OH minerals are weak to moderate with negative signs (−0.177962, −0.235635, and −0.434915, respectively) (Table 3). Therefore, ferrous iron oxides (Fe^{+2}) can be characterized as dark pixels due to the strong magnitude and negative sign of eigenvector loadings (−0.547623) in the DPCA2. Considering the eigenvector loadings in this DPCA (see Table 3), the contribution of other mineral groups as dark pixels, especially Si-OH minerals, is also feasible. These dark pixels were converted to bright pixels by multiplication to −1, and then a pseudocolor ramp of greyscale rule image was generated for the DPCA2. Figure 7A shows the resultant image-map of ferrous iron oxides (Fe^{+2}) and silica-rich units. Referring to the geological map of the study area, high to moderate concentration of ferrous oxides/Si-OH was mostly mapped in the sedimentary successions of the Franklinian Basin, which can be attributed to dolomite and basal siliciclastic rocks. In the Cu-Au mineralization belt, some small zones show a high to moderate spatial distribution of ferrous oxides/Si-OH components.

In the DPCA2, ferric iron (Fe^{+3}) oxide/hydroxides can be mapped explicitly as bright pixels due to strong and positive loadings of the B4/B2 (0.589087) (Table 3). Figure 7B shows the pseudocolor ramp of the DPCA2 for ferric iron components. High to moderate surface abundance of ferric iron components is typically detected at the contact of orthogneiss and paragneiss with the Franklinian sedimentary successions. However, high concentration of ferric iron was also mapped in association with orthogneiss and quartz diorite in the northeastern part of the selected subset near Dallas Bugt. Carbonate successions of the Franklinian Basin and paragneiss of the Etah Group generally show a moderate to high surface abundance of ferric iron in some parts of the selected subset (Figure 7B). Several small zones of high to moderate concentration of ferric iron were identified within the Cu-Au mineralization belt, which can be considered as gossan zones (rust zones). The 4/2 band ratio of ASTER was documented as a reliable indicator for identifying gossan zones associated with massive

sulfide mineralization in the Neoproterozoic Wadi Bidah shear zone, southwestern Saudi Arabia and many porphyry copper deposits around the world [99,100].
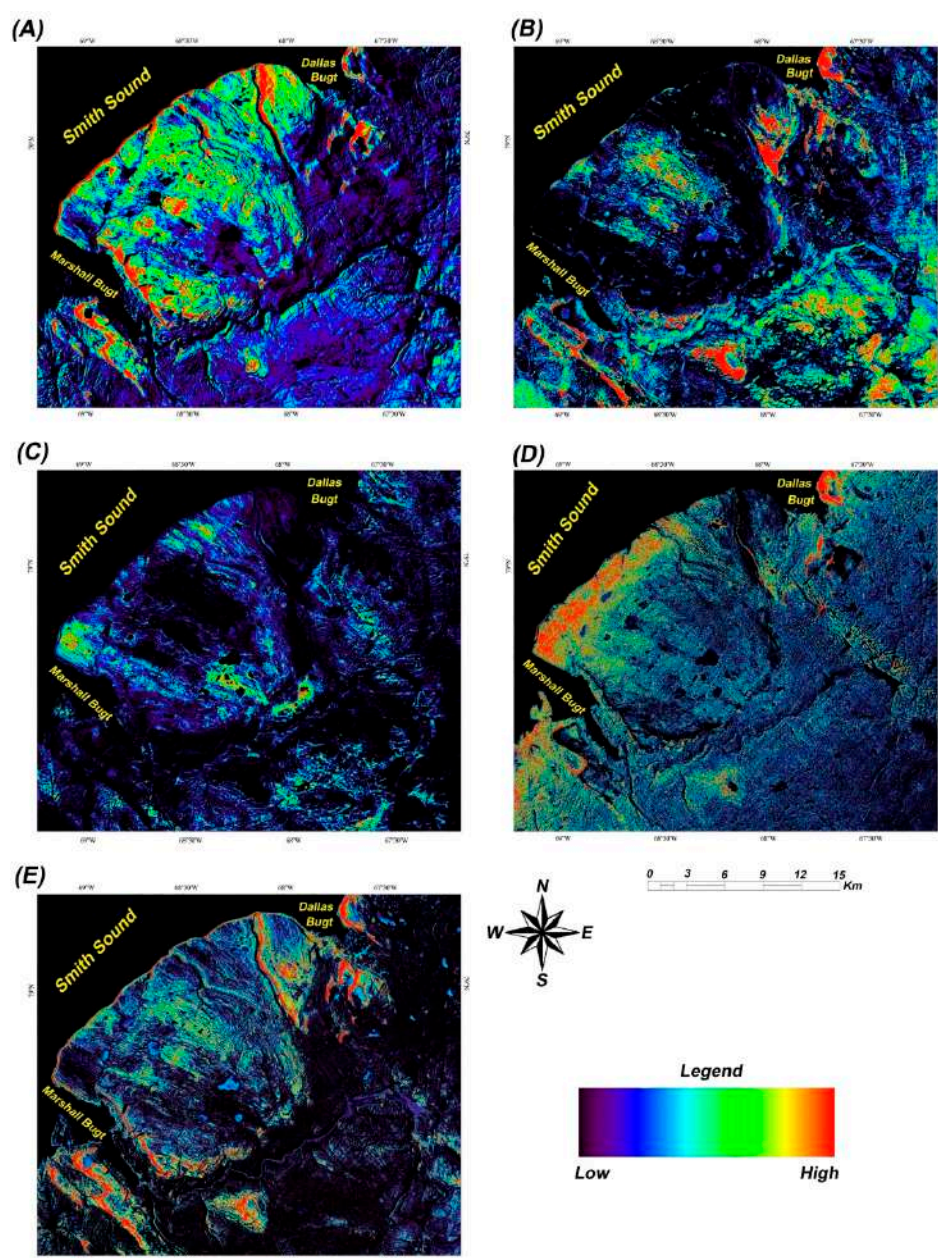

Figure 7. Pseudocolor ramp of the ASTER (VNIR + SWIR) DPCA rule images covering the selected spatial subset of the Cu-Au mineralization belt and surrounding areas. (**A**) Ferrous iron oxides (Fe^{+2})/Si-OH image-map; (**B**) ferric iron (Fe^{+3}) oxide/hydroxides image-map; (**C**) Al/Fe-OH minerals image-map; (**D**) Mg-Fe-OH minerals image-map; (**E**) Si-OH minerals image-map.

Al/Fe-OH minerals can be robustly detected in the DPCA3 image as dark pixels due to a high negative contribution of the B5+B7/B6 (−0.759215) (Table 3). For inverting the dark pixels to bright pixels, the DPCA3 image was negated. The pseudocolor ramp of the DPCA3 is shown in Figure 7C. The high concentration of Al/Fe-OH minerals was only mapped in some small sites in the carbonate/siliciclastic units of the Franklinian Basin, Quaternary deposits, quartz diorite, and amphibolite of the Etah Group. The orthogneiss and paragneiss units show low to moderate distribution of Al/Fe-OH minerals. The central part of the Cu-Au mineralization belt contains moderate to high spatial distribution of the mineral groups, which is related to the quartz diorite and

amphibolite units (Figure 7C). The DPCA4 contains strong loadings of B7 + B9/B8 (0.709489) and B5 + B7/B6 (0.531229) with a positive sign (Table 3). Therefore, Mg-Fe-OH minerals can be mapped as bright pixels in the DPCA4 image. Although, this image might have some contribution of Al/Fe-OH minerals due to great and positive eigenvector loading of the B5 + B7/B6 component. Figure 7D shows a pseudocolor ramp of the DPCA4 image. High spatial distribution of Mg-Fe-OH minerals is typically concentrated in the Franklinian sedimentary successions and paragneiss units proximate to Marshall Bugt. However, the orthogneiss and quartz diorite units adjacent to Dallas Bugt also contain a strong surface abundance of the mineral groups. Few small locations inside the Cu-Au mineralization belt comprise high concentrations of Mg-Fe-OH minerals that are associated with rust zones (Figure7D).

The B6 + B8/B7 component in the DPCA5 has strong weighting (−0.750756) with a negative sign, which can represent Si-OH minerals as dark pixels. Besides, the B2/B1 (ferrous iron oxides) shows high contribution (−0.568874) with a negative sign in the DPCA5 (Table 3). This image was negated for converting the dark pixels to bright pixels before applying pseudocolor ramp (Figure 7E). The resultant image-map shows spatial distribution of Si-OH minerals that may have some contribution of ferrous iron oxides. The high concentration of Si-OH minerals is characteristically mapped associated with quartz diorite and at the contact of orthogneiss and paragneiss with the Franklinian sedimentary successions. In the Cu-Au mineralization belt, the high concentration of Si-OH minerals was mapped in several localities associated with rust zones, especially in the southwestern part of the belt (Figure 7E).

Table 4 shows the eigenvector matrix of the ASTER TIR band ratio indices, including Quartz Index (QI) = 11 × 11/10 × 12, Carbonate Index (CI) = 13/14, and Mafic Index (MI) = 12/13 [81], for the selected subset covering the Cu-Au mineralization belt and surrounding areas. Considering eigenvector loadings for mapping altered silica-rich rocks (containing SiO2 group), it is evident that the DPCA2 is able to detect altered silica-rich rocks as bright pixels because of the strong contribution of QI (0.792423) with a positive sign. The CI (−0.302209) and MI (−0.097008) components contain weak contributions with a negative sign in the DPCA2 (Table 4). Figure 8A shows a pseudocolor ramp of the DPCA2 for the QI component. High to moderate concentration of quartz content was mostly mapped at the contact of orthogneiss with the Franklinian Basin successions, orthogneiss, and quartz diorite units. The low surface abundance of quartz was recorded for paragneiss and amphibolite. Several zones containing intense concentration of quartz content were identified in the Cu-Au mineralization belt (Figure 8A).

Table 4. Eigenvector matrix of the ASTER TIR band ratio indices derived from the DPCA for the selected subset covering the Cu-Au mineralization belt and surrounding areas.

Eigenvector	QI	CI	MI
DPCA 1	−0.596505	−0.527385	−0.605018
DPCA 2	0.792423	−0.302209	−0.097008
DPCA 3	−0.106481	0.790280	−0.530590

The DPCA3 shows strong loadings for the CI (0.790280) with a positive sign and the MI (−0.530590) with a negative sign, respectively (Table 4). Therefore, carbonate minerals can be detected as bright pixels and mafic minerals as dark pixels in the DPCA3 rule image. Figure 8B displays a pseudocolor ramp of the DPCA3 for the CI component. High to moderate concentration of carbonate minerals were identified in carbonate successions of the Franklinian Basin. The Etah meta-igneous complex (orthogneiss and quartz diorite) and the Etah Group (paragneiss and amphibolite) generally show a low to moderate surface abundance of carbonate minerals. The Cu-Au mineralization belt mostly locates in a low to moderate range of carbonate content zone (Figure 8B). Moreover, a pseudocolor ramp of the MI was generated using the negation of the DPCA3 rule image (Figure 8C). Quartz-rich zones (contact boundaries of sedimentary successions with metamorphic units) appear in a very low range of mafic content in the MI image-map (Figure 8C). Mafic minerals show high to moderate ranges in the entire image-map, which are mostly concentrated in the Franklinian Basin, paragneiss, and orthogneiss units (Figure 8C).
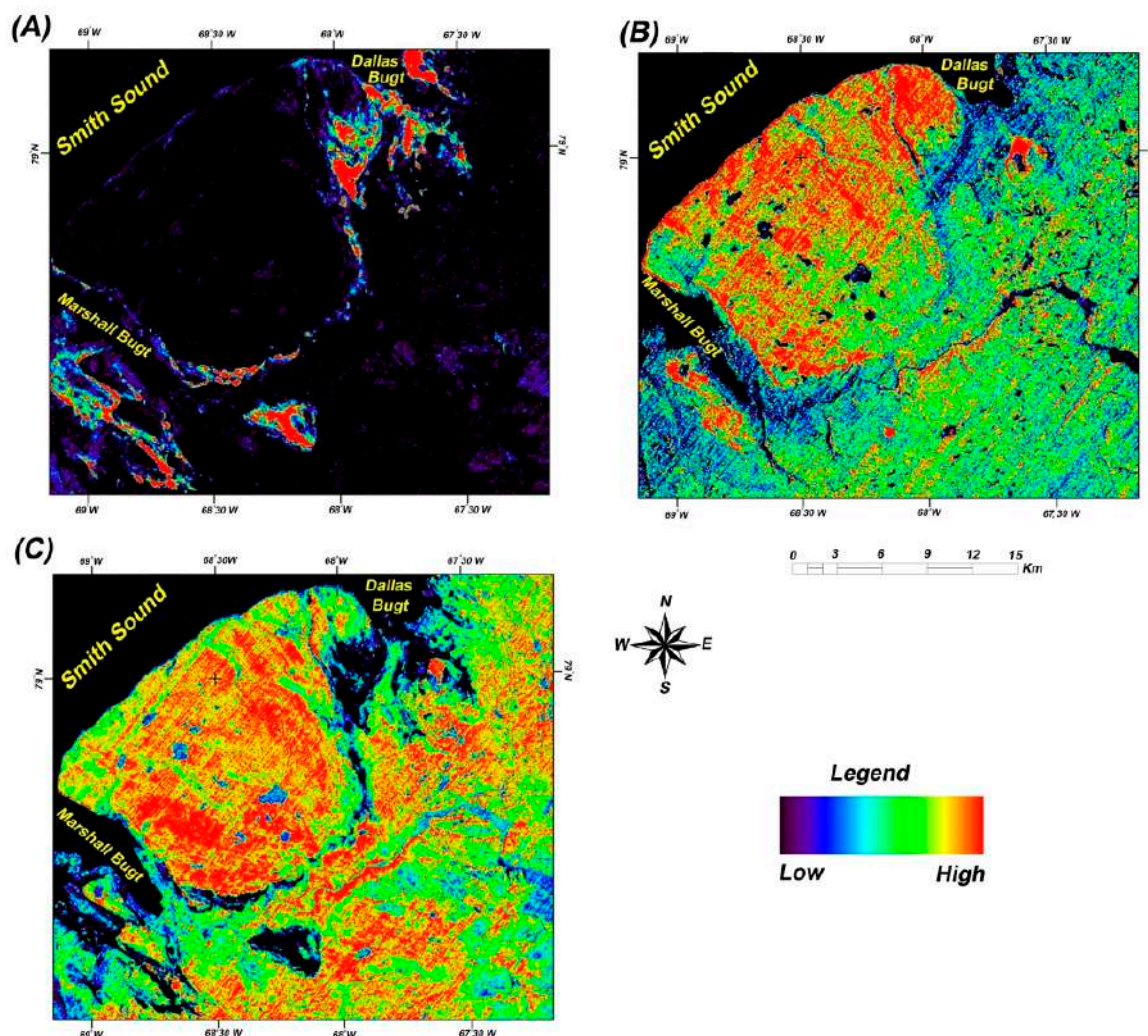
Figure 8. Pseudocolor ramp of the ASTER (TIR) DPCA rule images covering the selected spatial subset of the Cu-Au mineralization belt and surrounding areas. (**A**) Quartz Index (QI) image-map; (**B**) Carbonate Index (CI) image-map; (**C**) Mafic Index (MI) image-map.

The end-member spectra (n-D classes) extracted from the n-Dimensional analysis technique for the ASTER selected spatial subset covering the Cu-Au mineralization belt and surrounding areas are shown in Figure 9A. The n-D classes were compared with the end-member spectra of target minerals from the USGS spectral library (see Figure 3B). Results indicate that some of the n-D classes contain recognizable features similar to the target minerals. The n-D class #1 has an identical spectral signature with chalcedony and opal (see Figures 3B and 9A). Strong absorption features in bands 7, 8, and 9 could be attributed to Si-OH absorption characteristics. The n-D class #2 represents a combined spectral signature of jarosite and hematite due to Fe^{3+} (0.48 μm and 0.83–0.97 μm) and Fe-OH (2.27 μm) absorption features [90], coinciding with bands 1, 2, 3, and 7 of ASTER. The n-D class #3 and n-D class #5 do not contain any prominent spectral signatures related to the alteration minerals and can be considered as an unaltered/unknown mineral group. Snow/ice spectral signatures are recognizable in the n-D class #4 and n-D class #10 (Figure 9A). Strong reflectance in the VNIR portion (0.520–860 μm; bands 1, 2 and 3 of ASTER) and low reflectance in the SWIR portion (1.60–2.430 μm; bands 4 to 9 of ASTER) specify the snow/ice spectral properties [96]. The n-D class #6 contains spectral characteristics close to chlorite and epidote, which shows a dominant Mg, Fe-OH absorption at 2.30–2.35 μm [101] equivalent to bands 8 and 9 of ASTER. Biotite might be represented in the n-D class #7 because of slight iron absorption and a major Mg, Fe-OH absorption (Figure 9A). The n-D class #8 reveals mixed spectral features of hematite and jarosite. The n-D class #9 shows strong Al-OH spectral

absorption features at 2.20 μm [90], which is related to muscovite/kaolinite spectral signatures coinciding with band 6 of ASTER.

Figure 9B shows the LSU classification mineral map derived from fraction images of end-members (excluding snow/ice and unaltered/unknown groups) for the selected spatial subset covering the Cu-Au mineralization belt and surrounding areas. Results indicate that hematite/jarosite, muscovite/kaolinite, and biotite are spectrally strong, while chalcedony/opal and chlorite/epidote have a moderate contribution in total mixed spectral characteristics of the selected spatial subset. Comparison with the geological map of the study area (see Figure 1) suggests that muscovite/kaolinite is dominant in the Cu-Au mineralization belt, which is typically concentrated in the orthogneiss and amphibolite lithological units. In addition, a high surface abundance of biotite was mapped in both orthogneiss and paragneiss of the Etah meta-igneous complex and Etah group. The association of hematite/jarosite, chlorite/epidote, chalcedony/opal, and muscovite/kaolinite was identified in several parts of the central and southwestern sectors of the Cu-Au mineralization belt (Figure 9B), which are matched with the distribution of the main Cu-Au occurrences as documented by Pirajno et al. [2]. The Franklinian Basin sequences contain a high surface abundance of hematite/jarosite and chlorite/epidote and muscovite/kaolinite and a moderate to low surface abundance of chalcedony/opal and biotite. The high concentration of hematite/jarosite was mapped in the carbonate succession, while chlorite/epidote and muscovite/kaolinite were detected in the basal siliciclastic rocks. Chalcedony/opal is mostly concentrated at the contact between the Franklinian Basin sequences and Etah meta-igneous complex and Etah group. Low spatial distribution of biotite was detected in the basal siliciclastic rocks of the Franklinian Basin sequences (Figure 9B).
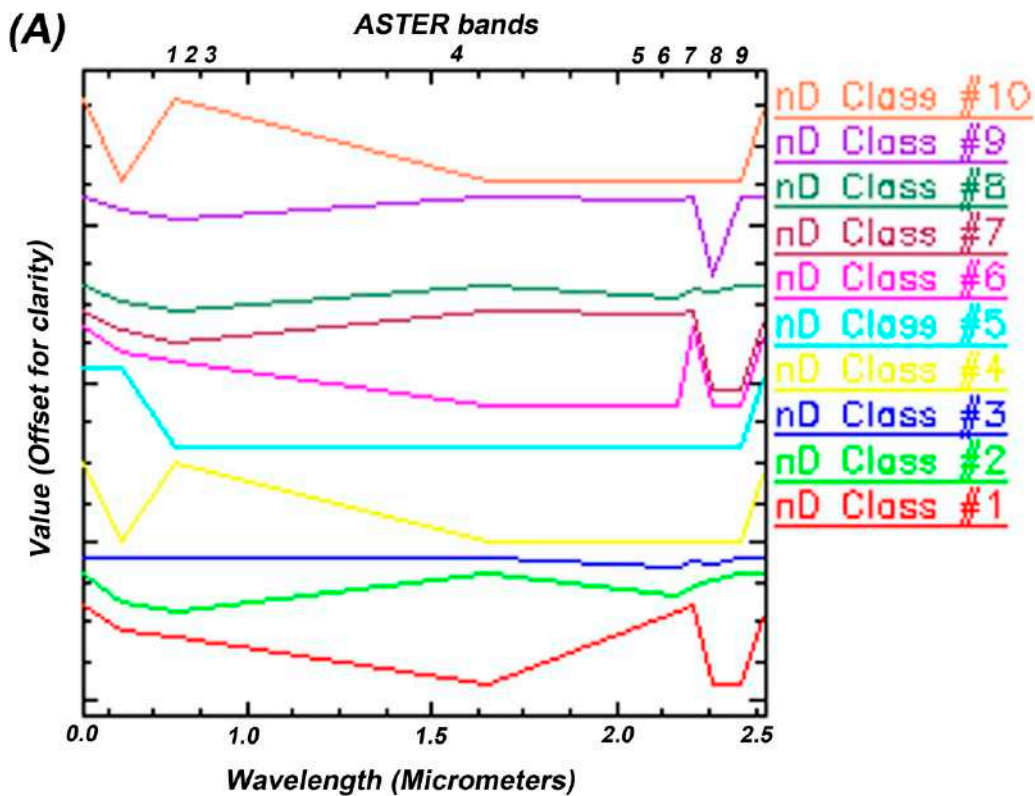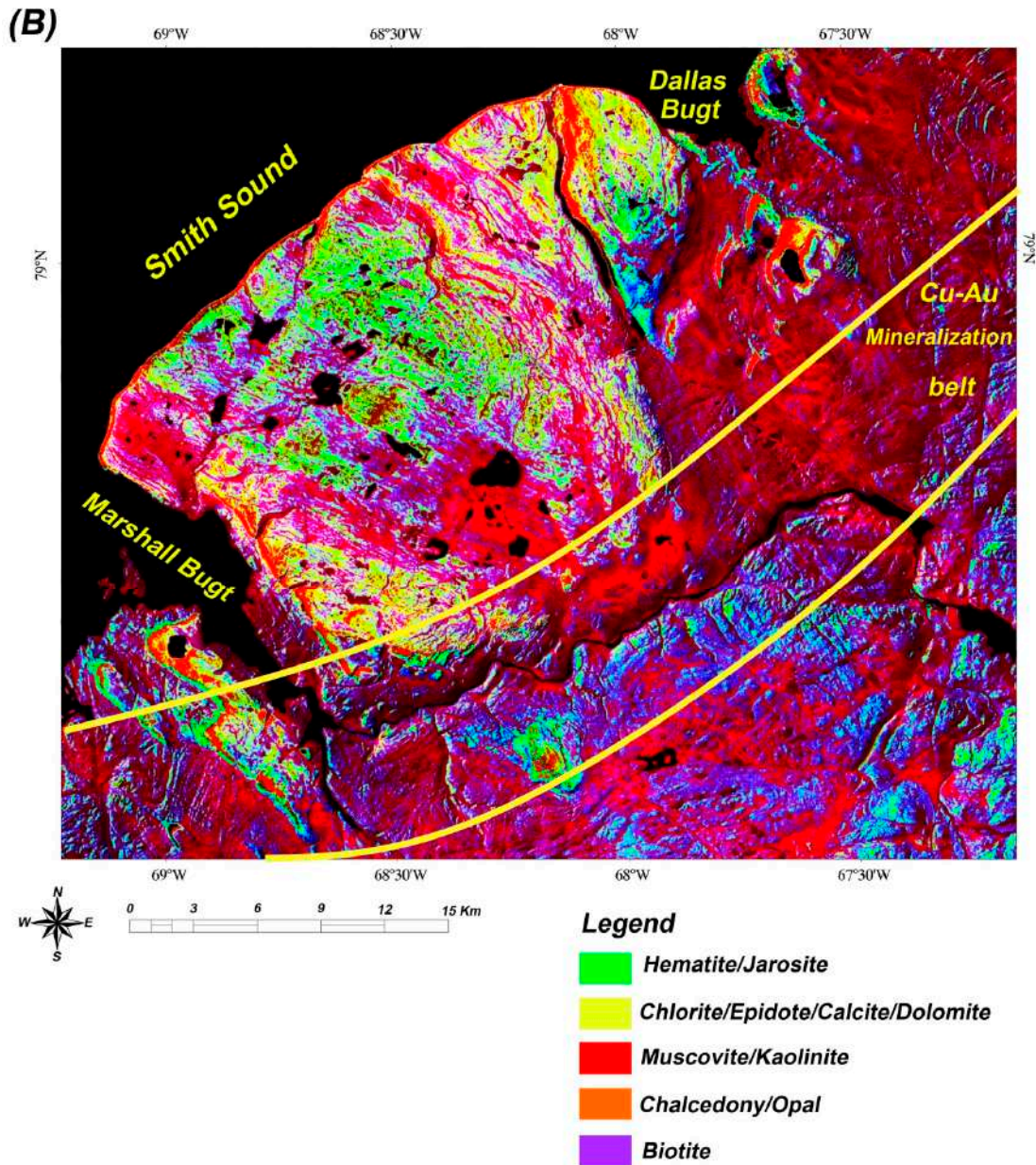
Figure 9. (**A**) The n-D classes (end-member spectra) extracted for a selected spatial subset (ASTER VNIR + SWIR) covering the Cu-Au mineralization belt and surrounding areas. ASTER band center positions are shown. (**B**) ASTER LSU classification mineral map for the selected spatial subset covering the Cu-Au mineralization belt and surrounding areas.

4.3. Mapping Iron Oxide/Hydroxide Minerals in the Southern Part of the Cu-Au Mineralization Belt Using WV-3 Data

A spatial selected subset of WV-3 imagery covering the southern part of the Cu-Au mineralization belt was considered (Figure 10) for mapping Fe^{3+} and Fe^{2+} iron oxides and ferric and ferrous silicates. Table 5 shows the eigenvector matrix of the WV-3 band ratio indices derived from the DPCA analysis, including B4 + B2/B3 (for mapping Fe^{3+} iron oxides), B6 + B8/B7 (for mapping Fe^{2+} iron oxides), B3 + B5/B4 (for mapping ferric silicates), and B5 + B7/B6 (for mapping ferrous silicates). The DPCA1 does not contain any specific contribution of band ratio indices with different signs (all of the eigenvector loadings are negative). Thus, this image-map contains spectral similarities and does not enhance any group of target minerals. The DPCA2 shows strong and positive eigenvector loading for mapping Fe^{3+} iron oxides (0.762743). However, the eigenvector loading for Fe^{2+} iron oxides (−0.369967) is weak and negative. The ferric (0.461865) and ferrous (0.262084) silicates have moderate

to weak contribution with positive signs in the DPCA2 image. Therefore, the DPCA2 image-map represents the Fe^{3+} iron oxides as bright pixels, which might contain a very low contribution of ferric and ferrous silicates. Figure 10A shows a pseudocolor ramp of the DPCA2 covering the southern part of the Cu-Au mineralization belt, which includes two Cu-Au mineralization occurrences that have been already documented by Pirajno et al. [2]. High to moderate concentration of Fe^{3+} iron oxides is mapped in the vicinity of Cu-Au mineralization occurrences (Figure 10A). Moreover, many other parts inside the Cu-Au mineralization belt show strong to moderate spatial distribution of Fe^{3+} iron oxides (Figure 10A), which could be considered as high potential zones for Cu-Au mineralization.

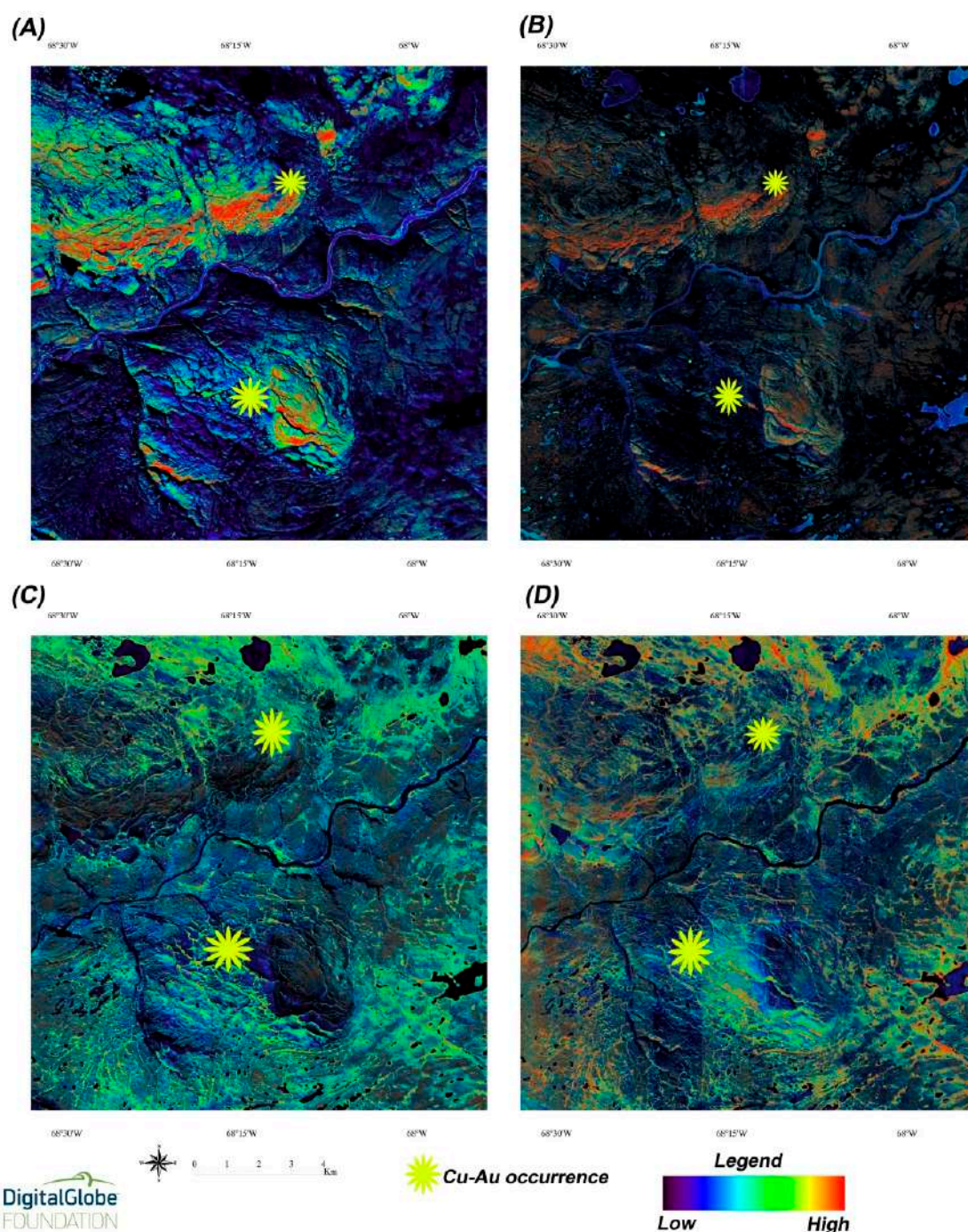**Figure 10.** Pseudocolor ramp of the WV3 (VNIR) DPCA rule images covering the selected spatial subset of the southern part of the Cu-Au mineralization belt. (**A**) Fe^{3+} iron oxides image-map; (**B**) Fe^{2+} iron oxides image-map; (**C**) ferric silicates image-map; (**D**) ferrous silicates image-map (WV-3 image, courtesy of the DigitalGlobe Foundation (www.digitalglobefoundation.org)).

Table 5. Eigenvector matrix of the WV-3 band ratio indices derived from the DPCA for the selected subset covering the southern part of Cu-Au mineralization belt.

| Eigenvector	B4 + B2/B3	B6 + B8/B7	B3 + B5/B4	B5 + B7/B6
DPCA 1	−0.155644	−0.927722	−0.174958	−0.290683
DPCA 2	0.762743	−0.369967	0.461865	0.262084
DPCA 3	0.049338	−0.949469	0.090503	0.396450
DPCA 4	0.496839	−0.004738	−0.864801	0.072448

The DPCA3 contains a significant contribution of Fe^{2+} iron oxides (−0.949469) and very low eigenvector loading of Fe^{3+} iron oxides (0.049338) and ferric silicates (0.090503), while a moderate contribution of ferrous silicates (0.396450) with a positive sign is present in this DPCA. Hence, the Fe^{2+} iron oxides will appear as dark pixels. The DPCA3 was negated (multiplication by −1) to generate the Fe^{2+} iron oxides as bright pixels. A pseudocolor ramp of the DPCA3 was generated to map Fe^{2+} iron oxides (Figure 10B). The high surface abundance of Fe^{2+} iron oxides was also detected proximate to the mineralization localities. For mapping ferrous silicates, a pseudocolor ramp was applied to the DPCA3 without negation (Figure 10C). Spatial distribution of ferrous silicates can be seen in many parts of the selected subset, especially in drainage systems and geological structures. However, a low concentration of the ferrous silicates is mapped close to the Cu-Au mineralization occurrences (Figure 10C).

The DPCA4 has a strong negative eigenvector loading of ferric silicates (−0.864801) and moderate positive contribution of Fe^{3+} iron oxides (0.496839), whereas eigenvector loadings for Fe^{2+} iron oxides (−0.004738) and ferrous silicates (0.072448) are meager. As a result, the ferric silicates will manifest as dark pixels in the DPCA4, which could be inverted to bright pixels by negation. The moderate contribution of Fe^{3+} iron oxides can affect the resultant map. Figure 10D shows a pseudocolor ramp for ferric silicates. In many parts, the surface abundance of ferric silicates is much stronger compared to ferrous silicates, especially adjacent to Cu-Au mineralization occurrences. The high concentration of ferric silicates shows a close spatial relationship with Fe^{3+} and Fe^{2+} iron oxides. The high to moderate surface abundance of ferric silicates was mapped nearby the Cu-Au mineralization localities in the selected subset (Figure 10D).

End-member spectra (n-D classes) extracted from the n-Dimensional analysis technique for the WV-3 selected spatial subset of the southern part of the Cu-Au mineralization belt are presented in Figure 11A. Comparison with selected end-member reflectance spectra of the target minerals from the USGS spectral library (see Figure 3C) shows the presence of some n-D classes containing similar spectral characteristics with hematite, jarosite, ferric, and ferrous silicates. The n-D class #1, n-D class #3, n-D class #5, and n-D class #8 do not contain any particular spectral signature related to alteration minerals, which might be water/ice (snow/slush) or unknown geologic materials. The concentration of transition metal cations such as Fe^{3+} and Fe^{2+} can affect the intensities of absorption features [100]. Fe^{3+} produces absorption features near 0.45 to 0.90 μm, while broad absorption features near 0.90 to 1.2 μm are related to Fe^{2+} [101]. The n-D class #2 has absorption features related to ferric iron (Fe^{3+}), which corresponds with bands 5 (Red), 6 (Red edge), and 7 (Near-Infrared 1) of WV-3. It seems that this n-D class is related to ferric silicates. The n-D class #4 shows a similar spectral pattern with hematite (see Figures 3C and 11A). The n-D class #6 can be considered for jarosite. The n-D class #7 can be attributed to the admixture of hematite and jarosite. Charge transfer absorption features between 0.48 to 0.72 μm and crystal-field absorption properties between 0.63 to 0.72 μm are documented for iron oxide/hydroxide minerals such as hematite, limonite, goethite, and jarosite [102–104]. The n-D class #9 contains robust absorption features related to Fe^{2+}, coinciding with bands 7 (Near-Infrared 1) and 8 (Near-Infrared 2) of WV-3. Hence, it can be characterized by ferrous silicate.

The LSU spectral mineral-map of the WV-3 spatial selected subset covering the southern part of the Cu-Au mineralization belt was generated using fraction images derived from the n-D classes contain end-member reflectance spectra of the target minerals. Figure 11B shows the resultant image-map. In the vicinity of Cu-Au mineralization occurrences, high concentration of hematite, jarosite, and ferric silicates was identified. On the other hand, carbonates (calcite and dolomite) also appear

in association with ferric silicate, especially in the central and northwestern parts of the selected subset. Most of the ferrous silicates are detected in the drainage systems and geological structures.
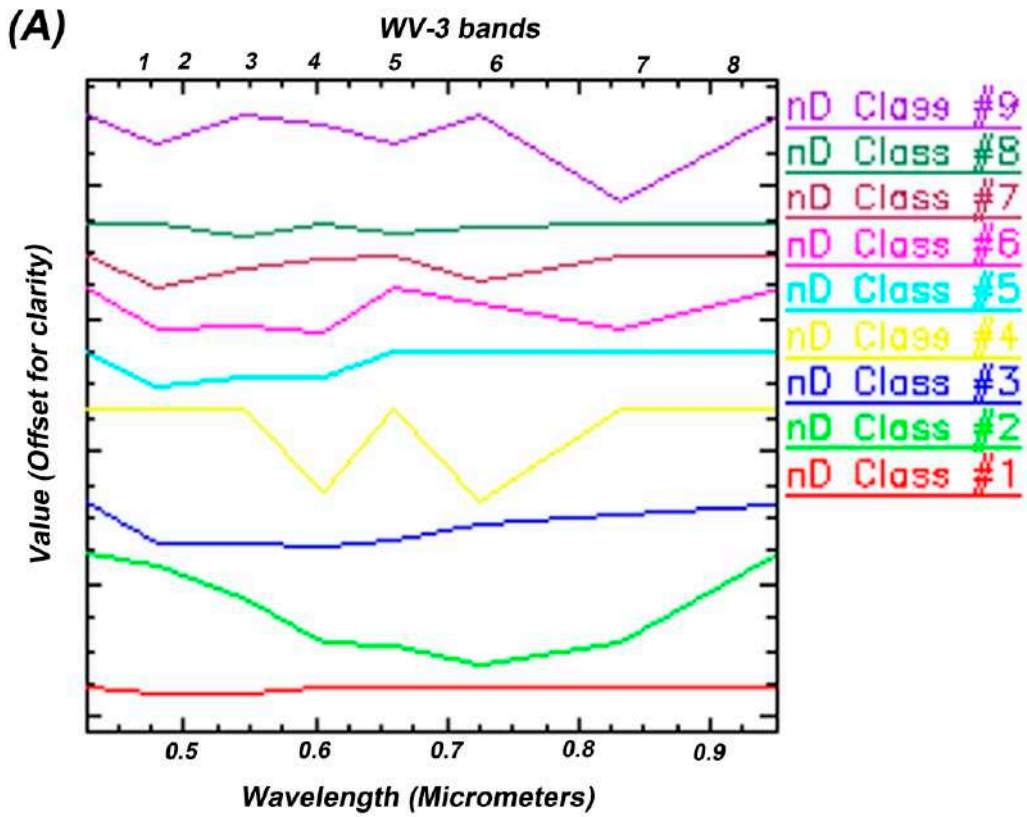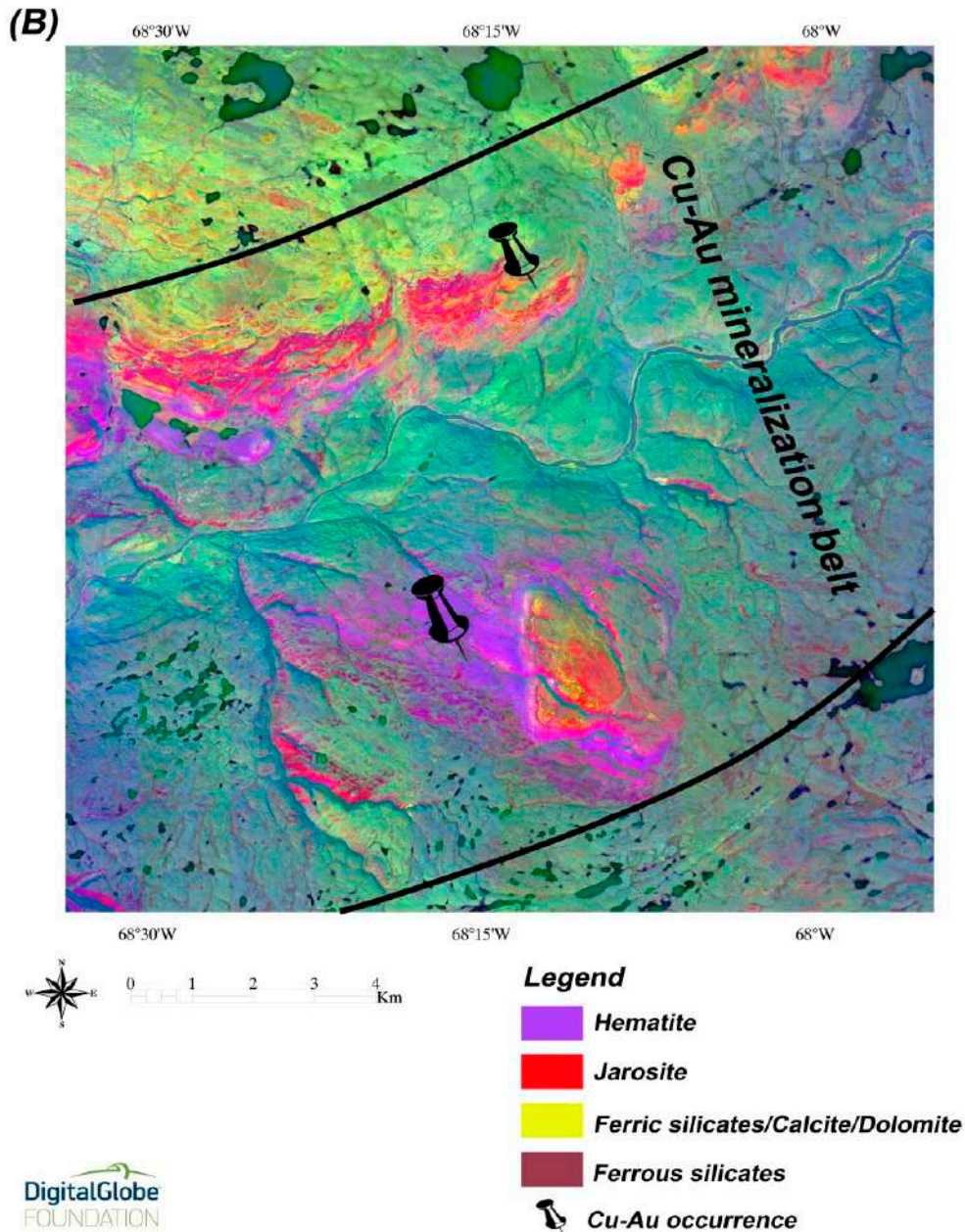
Figure 11. (**A**) The n-D classes (end-member spectra) extracted for the WV-3 selected spatial subset covering the southern part of the Cu-Au mineralization belt. WV-3 band center positions are shown. (**B**) LSU mineral map produced from fraction images for the selected spatial subset covering the southern part of the Cu-Au mineralization belt (WV-3 image, courtesy of the DigitalGlobe Foundation (www.digitalglobefoundation.org)).

4.4. ACE Analysis for Detecting End-Member Minerals Using VINR + SWIR Bands of ASTER

For verifying the presence of mineral spectral signatures detected in the selected spatial subset covering the Cu-Au mineralization belt and surrounding areas, the ACE algorithm was applied to the VINR + SWIR bands of ASTER using laboratory reflectance spectra of hematite, jarosite, biotite, muscovite, chlorite, epidote, chalcedony (hydrous-silica), and opal (hyalite) extracted from the USGS spectral library [75]. Fraction images of the selected end-member were generated as a series of greyscale rule images using the ACE algorithm. To show the high fractional abundance (high DN value pixels) of the target minerals, a pseudo-color ramp of greyscale rule images was produced, one for each selected mineral (Figure 12). The ACE image-maps were visually compared with the LSU classification image-maps (see Figures 6B, 9B, 11B and 12). Results indicate that fractional abundances

of hematite, chlorite, epidote, chalcedony, and opal are high, whereas jarosite and biotite are low in the detected altered zones. Spatial distribution of muscovite is typically different from other target minerals in the identified altered zones and selected subset (Figure 12). However, some of the high abundance zones contain jarosite, chalcedony, and opal that are spatially matched with muscovite. Comparison of the DPCA image-maps and LSU classification image-map of ASTER (see Figures 7 and 9B) with the ACE fraction images indicates a little spatial dissimilarity between the DPCA4 image (Figure 7D) for mapping Mg-Fe-OH minerals and fraction images of biotite, chlorite, and epidote (Figure 12). However, the LSU classification image-map (Figure 9B) shows a high spatial similarity with fraction images of hematite, jarosite, biotite, muscovite, chlorite, epidote, chalcedony, and opal.
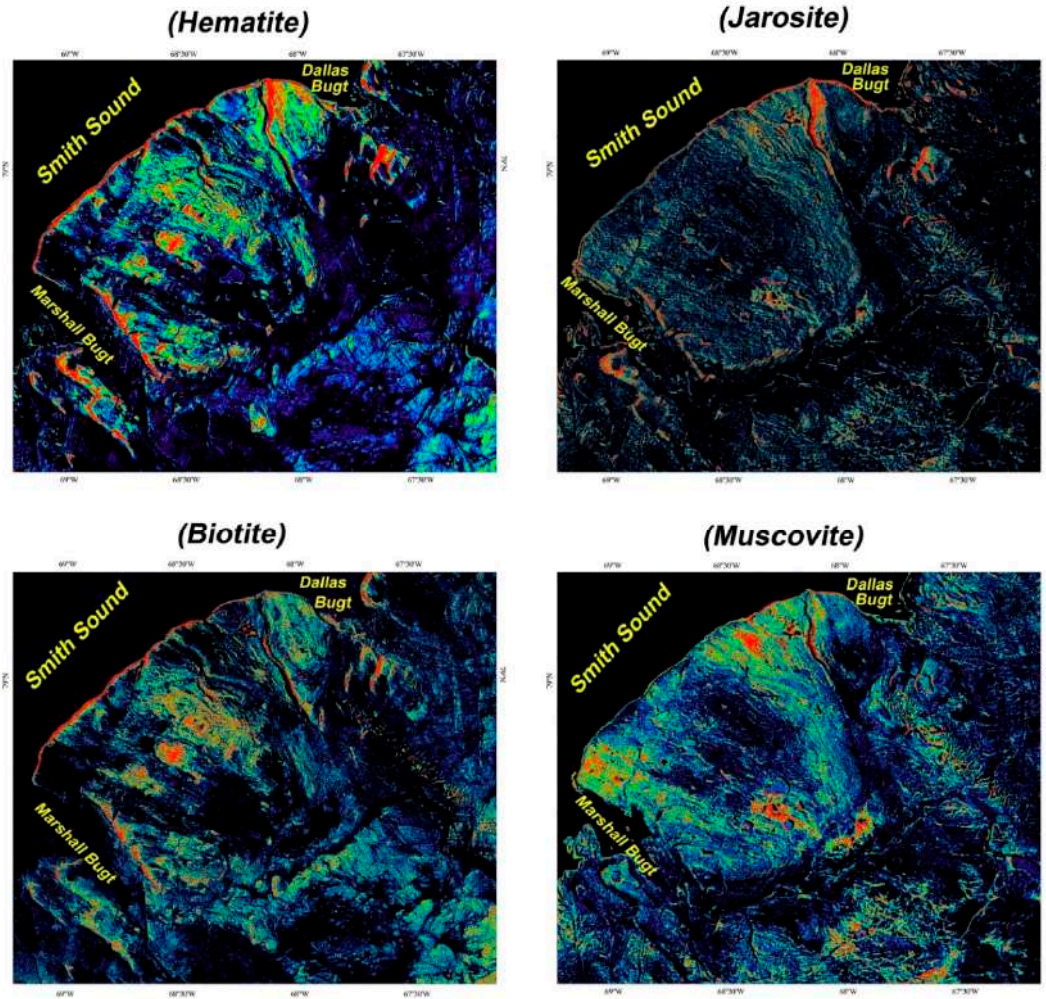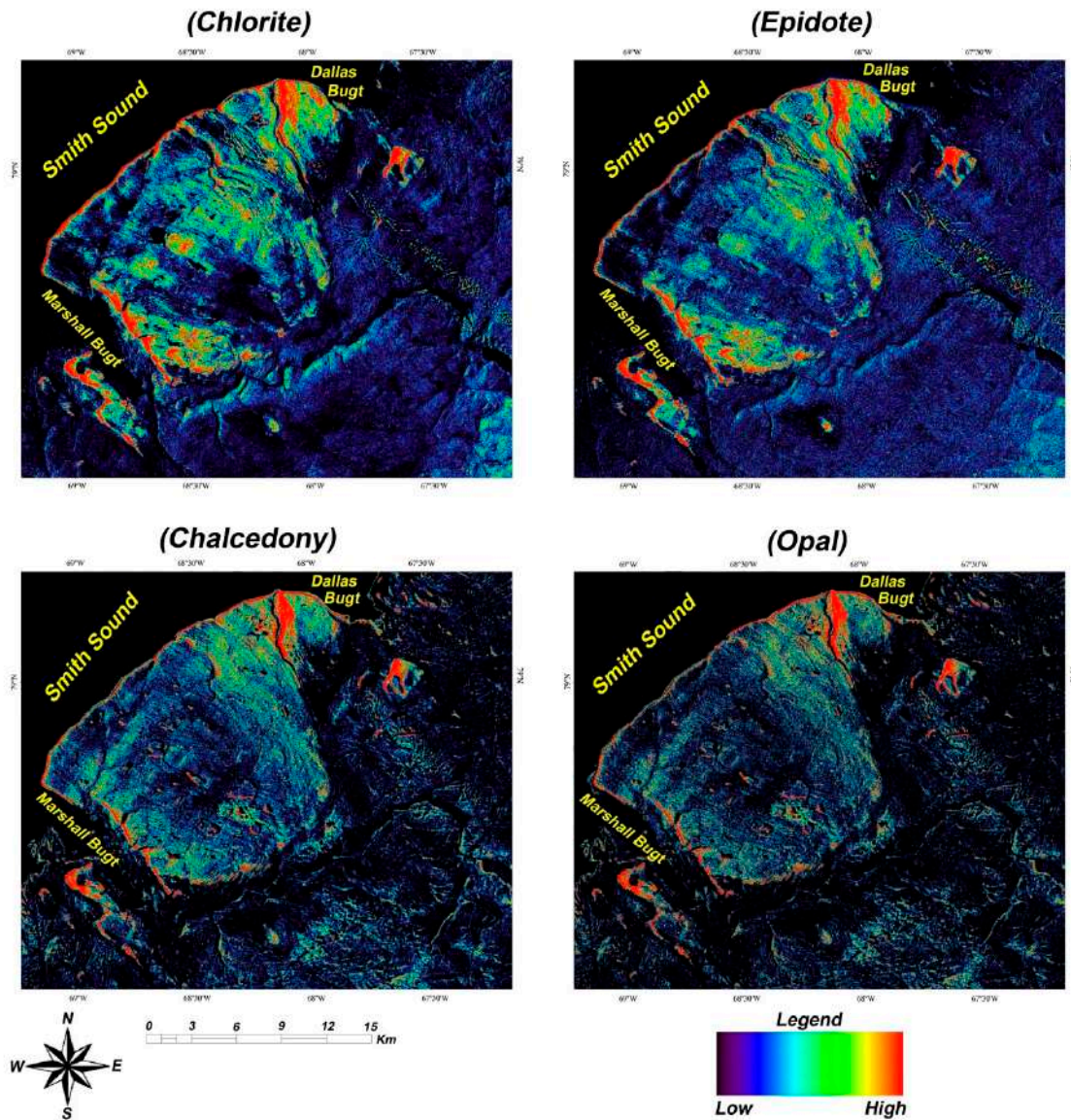
Figure 12. Fraction images of the selected end-member minerals derived from the adaptive coherence estimator (ACE) algorithm for the selected spatial subset covering the Cu-Au mineralization belt and surrounding areas. Pseudo-color ramp was applied to greyscale rule images.

4.5. Virtual Verification Assessment

Confusion matrix (error matrix) and Kappa Coefficient [102–104] were calculated for the LSU classification image-maps derived from Landsat-8, ASTER, and WV-3 versus the ACE fraction images derived from VINR + SWIR bands of ASTER (Tables 6–8). In this analysis, the confusion matrix was assumed based on one-class per pixel classifications. The pixels were selected inside the altered zones with high digital number values. The spatial resolutions of the pixels were considered and resampled to a similar size to the ACE fraction images using a pixel aggregation (neighborhood averaging). Furthermore, highly dissimilar pixels were excluded using a standard deviation threshold. Finally, 160 pixels of Landsat-8, 300 pixels of ASTER, and 200 pixels of WV-3 were selected and analyzed, respectively (Tables 6–8).

Table 6. Confusion matrix for the LSU classification image-maps derived from Landsat-8 versus the ACE fraction images derived from VINR + SWIR bands of ASTER.

LSU Classification Map Landsat-8	Detected Pixel Spectra by the ACE Algorithm				
	Iron Oxide/Hydroxides	Clay Minerals	Ferrous Silicates	Totals	User's Accuracy
Iron oxide/hydroxides	46	2	8	56	82%
Clay minerals	2	48	4	54	88%
Ferrous silicates	12	10	28	50	56%
Totals	60	60	40	160	
Producer's Accuracy	76%	80%	70%		
Overall accuracy = 76.25%			Kappa Coefficient = 0.64		

Table 7. Confusion matrix for the LSU classification image-maps derived from ASTER versus the ACE fraction images derived from VINR + SWIR bands of ASTER.

LSU Classification Map ASTER	Detected Pixel Spectra by the ACE Algorithm						
	Hematite/Jarosite	Chlorite/Epidote	Muscovite/Kaolinite	Chalcedony/Opal	Biotite	Totals	User's Accuracy
Hematite/jarosite	42	8	3	10	8	71	59%
Chlorite/epidote	6	39	1	7	6	59	66%
Muscovite/kaolinite	0	1	43	2	5	51	84%
Chalcedony/opal	7	8	8	38	6	67	56%
Biotite	5	4	5	3	35	52	67%
Totals	60	60	60	60	60	300	
Producer's Accuracy	70%	65%	71%	63%	58%		
Overall accuracy = 65.66%			Kappa Coefficient = 0.57				

Table 8. Confusion matrix for the LSU classification image-maps derived from WV-3 versus the ACE fraction images derived from VINR + SWIR bands of ASTER.

LSU Classification Map WV-3	Detected Pixel Spectra by the ACE Algorithm					
	Hematite	Jarosite	Ferric Silictes	Ferrous Silicates	Totals	User's Accuracy
Hematite	39	6	5	1	51	76%
Jarosite	7	40	4	3	54	74%
Ferric Silictes	3	4	38	9	54	70%
Ferrous Silicates	1	0	3	37	41	90%
Totals	50	50	50	50	200	
Producer's Accuracy	78%	80%	76%	74%		
Overall accuracy = 77%			Kappa Coefficient = 0.69			

Table 6 shows confusion matrix for the LSU classification image-maps derived from Landsat-8 versus the ACE fraction images derived from VINR + SWIR bands of ASTER. The overall accuracy and Kappa Coefficient are 76.25% and 0.64, respectively. Producer's accuracy (omission error) indicates the probability of a reference pixel being correctly classified and user's accuracy (commission error) shows the total number of correct pixels in a category, which is divided by a total number of pixels that were classified in the category [105,106]. The highest producer's accuracy (80%) and user's accuracy (88%) were achieved for the clay minerals class. However, the lowest producer's accuracy (70%) and user's accuracy (56%) were recorded for the ferrous silicates class. It shows that spectral mixing and confusion between the ferrous silicates and iron oxide/hydroxides classes is more feasible than the clay minerals class using Landsat-8 spectral bands.

The overall accuracy of 65.66% and Kappa Coefficient of 0.57 were assessed for the LSU classification image-maps versus the ACE fraction images derived from VINR + SWIR bands of ASTER (Table 7). The muscovite/kaolinite class has the highest producer's accuracy (71%) and user's accuracy (84%). The biotite class shows the lowest producer's accuracy (58%) and the chalcedony/opal class contains the lowest user's accuracy (56%). So, the muscovite/kaolinite class pixels were strongly mapped compared to other mineral classes in this study. Spectral mixing has been recorded for pixels contain hematite/jarosite, chlorite/epidote, chalcedony/opal, and biotite mineral assemblages. Consequently, detecting the subtle spectral differences between alteration mineral classes are challenging and might have some confusion using ASTER data. Calculation of confusion matrix for LSU classification image-maps derived from WV-3 versus the ACE fraction images derived from VINR + SWIR bands of ASTER indicates the overall accuracy of 77% and Kappa

Coefficient of 0.69 (Table 8). Producer's accuracy and user's accuracy for ferrous silicates class pixels are 74% and 90%, respectively. The jarosite class pixels contain the highest producer's accuracy (80%). The ferric silicates class pixels show the lowest user's accuracy (70%). Results indicate some spectral mixing effects between mineral classes, but the overall accuracy (77%) and Kappa Coefficient (0.69) have a good potential for separating the classes using WV-3 VNIR spectral bands.

5. Discussion

Mineral exploration is very challenging in the Arctic regions due to cold and harsh environments and inaccessibility, especially in the northern part of Greenland that contains a variety of ore mineral resources [3,105]. Application of remote sensing satellite/airborne imagery for mineral identification, exploration, and prospecting in Greenland has been documented in the Sarfartoq carbonatite complex, southern West Greenland [106,107] and the Kap Simpson complex area, East Greenland [108] as well as the Franklinian Basin, North Greenland [8]. The Inglefield Mobile Belt (IMB), Northwest Greenland contains copper-gold mineralization hosted by garnet-sillimanite paragneiss, orthogneiss, and mafic-ultramafic rocks, which are confined in hydrothermal alteration zones (rust zones) [1–3]. In this study, the application of Landsat-8, ASTER, and WV-3 multispectral satellite remote sensing data were evaluated for mapping hydrothermal alteration minerals associated with Cu-Au mineralization in the IMB.

Using ratio indices of Landsat-8 spectral bands (B4/B2, B4/B6, and B6/B7) discriminate a variety of sedimentary, metamorphic, and igneous lithological units at the regional scale based on different content of iron oxides/hydroxides, ferrous iron oxides, and hydroxyl minerals (see Figure 5A). The sedimentary successions of the Franklinian Basin and Thule Supergroup were mapped due to high amounts of Al-OH, Mg-Fe-OH, CO_3, and Si-OH mineral groups related to carbonate and siliciclastic rocks and Fe^{2+} absorption that might be attributed to dolomitization. Basaltic sills of the Thule Basin, paragneiss of the Etah Group, and syenite and orthogneiss of the Etah meta-igneous complex were discriminated because of different surface abundance of Fe^{3+} and Fe^{2+} iron oxides/hydroxide minerals (see Figure 5A). Quaternary deposits were mapped owing to the high surface distribution of detrital clay minerals. The DPCA3 and DPCA4 images derived from Landsat-8 band ratio indices identified Fe^{3+}/Fe^{2+} iron oxides/hydroxide minerals and Al-OH, Mg-Fe-OH, CO_3, and Si-OH alteration mineral groups, respectively (see Figure 5B,C).

In the DPCA3 image-map (Figure 5B), the boundaries between the Etah metamorphic complex rocks and sedimentary successions of the Franklinian Basin and Thule Supergroup in the Central Terrane, as well as the southern part of the Cu-Au mineralization belt nearby Marshall Bugt, show high surface abundance of iron oxide/hydroxide minerals. These locations are typically matched with the documented rust zones, which are identified as Cu-Au sulfide mineralization areas [1–3]. Furthermore, a high concentration of the OH-alteration mineral groups was mapped in the DPCA4 image-map (see Figure 5C) that could be considered with some parts of the rust zones. The XRD analyses, as documented by Pirajno et al. [2] for mineralogy of rust zones indicate the presence of biotite, sericite, and chlorite. High spatial distribution of iron oxide/hydroxide minerals along the boundaries between the metamorphic complex rocks and sedimentary successions in the southwestern part of the Cu-Au mineralization belt was also detected in the LSU spectral mineral-map of the Landsat-8 (see Figure 6B). Ferrous silicates (biotite, chlorite, and epidote) were typically mapped with iron oxide/hydroxide minerals, while clay minerals, detected in the central part of the Cu-Au mineralization belt, are mostly adjacent to the amphibolite and quartz diorite lithological units (see Figures 1 and 6B).

Detailed maps of the spatial distribution of Fe^{3+}/Fe^{2+} iron oxide/hydroxides, Al/Fe-OH, Mg-Fe-OH, and Si-OH minerals in the Cu-Au mineralization belt and surrounding areas (see Figure 7) were generated by implementing the DPCA technique to ASTER band ratio components (B2/B1, B4/B2, B5 + B7/B6, B7 + B9/B8, and B6 + B8/B7). The DPCA2 mapped the Fe^{3+}/Fe^{2+} iron oxide/hydroxide minerals, which are highly concentrated at the contact of metamorphic complex rocks with the Franklinian sedimentary successions and orthogneiss in the northeastern and southern parts of the Cu-Au mineralization belt (see Figure 7A,B). Numerous zones of high to moderate concentration of iron

oxide/hydroxide minerals were mapped inside the Cu-Au mineralization belt together with the rust zones. The occurrence of iron minerals such as rozenite, jarosite, cacoxenite, and jahnsite was reported in the Cu-Au mineralization belt as oxidation products of sulfide minerals associated with the rust zones [2]. The DPCA3 and DPCA4 images represented the spatial distribution of Al/Fe-OH and Mg-Fe-OH minerals, which show low abundances in the mineralization belt (Figure 7C,D). The DPCA5 detected Si-OH minerals and ferrous silicates, which are typically associated with quartz diorite and the contact between metamorphic complex rocks with the Franklinian sedimentary successions (Figure 7E). The high concentration of Si-OH minerals was mapped as associated with rust zones, particularly in the southwestern part of the mineralization belt. Pirajno et al. [2] documented the association of hydrolitic alteration assemblages (chlorite and biotite) and silicification that overprint the wallrocks and rust zones in the Cu-Au mineralization belt.

The implementation of the DPCA to ASTER TIR band ratio indices (QI, CI, and MI) provided complementary information for mapping of altered, silica-rich rocks (containing SiO_2 group), carbonates, and mafic minerals in the DPCA2 and DPCA3 (Figure 8A–C). The boundaries of orthogneiss with the Franklinian Basin successions and quartz diorite units show a high to moderate concentration of quartz content, which is matched with the DPCA5 derived from the ASTER VNIR + SWIR ratio indices (see Figure 7E). In the Cu-Au mineralization belt, several zones containing high concentration of quartz content were identified (see Figure 8A). Carbonate minerals were clearly detected in carbonate successions of the Franklinian Basin, while mafic minerals were mostly mapped in the paragneiss and orthogneiss units (see Figure 8A,B). Boundaries of sedimentary successions with metamorphic rocks show a very low range of carbonates and mafic minerals. According to Pirajno et al. [1,2] and Kolb et al. [3] Cu–Au mineralization in rust zones is restricted to the NE-trending strip, which has a close spatial relationship with the contact of carbonate successions of the Franklinian Basin and the basement metamorphic rocks.

Hematite/jarosite, muscovite/kaolinite, and biotite are spectrally dominated in the ASTER LSU classification mineral map (Figure 9A), whereas chalcedony/opal and chlorite/epidote have a moderate contribution in the total mixed spectral properties. The assemblage of hematite/jarosite, chlorite/epidote, chalcedony/opal, and muscovite/kaolinite was detected in many parts of the Cu-Au mineralization belt (Figure 9B), especially in the central and southwestern parts, where the main occurrences of Cu-Au mineralization were reported by Pirajno et al. [2]. Muscovite/kaolinite has a high surface abundance in the Cu-Au mineralization belt, which is typically concentrated in the orthogneiss and amphibolite lithological units. Chalcedony/opal is generally concentrated at the contact between the Franklinian Basin sequences and basement metamorphic complex (Figure 9B). The spatial distribution of the alteration minerals in the ASTER LSU classification image-map was comparable with ASTER DPCA image-maps, however, a detailed surface abundance of alteration minerals was more apparent in the LSU classification image-map (see Figures 7A–E and 9B).

Fe^{3+} and Fe^{2+} iron oxides and ferric and ferrous silicates were comprehensively mapped in the southern part of the Cu-Au mineralization belt by applying DPCA to WV-3 band ratio indices (see Figure 10 and Table 5). High to moderate surface abundance of Fe^{3+} iron oxides was mapped near to Cu-Au mineralization occurrences (reported by Pirajno et al. [2]) in the DPCA2 image-map (Figure 10A). Furthermore, ferric silicates and Fe^{2+} iron oxides were also mapped in the vicinity of Cu-Au mineralization occurrences, which are recorded in the DPCA3 and DPCA4 image-maps (Figure 10B–D). A number of zones containing high to moderate spatial distribution of Fe^{3+} and Fe^{2+} iron oxides and ferric silicates are recorded as feasible Cu-Au mineralization occurrences. The LSU spectral mineral-map of the WV-3 shows spatial distribution of hematite, jarosite, ferric silicates/calcite/dolomite, and ferrous silicates (see Figure 11B). The high concentration of hematite, jarosite, and ferric silicates was mapped in the vicinity of Cu-Au mineralization occurrences, which is coincident with the DPCA image-map (see Figure 10). As stated by Pirajno et al. [2], the whole-rock XRD analyses of the rust zones have shown hydrous Fe sulfate and phosphate, jarosite, biotite, sericite, and chlorite, which are paralleled with the remote sensing results derived from WV-3 VNIR data.

The presence of hematite, jarosite, biotite, muscovite, chlorite, epidote, chalcedony, and opal in the selected spatial subset covering the Cu-Au mineralization belt and surrounding areas was verified using the ACE fraction images (see Figure 12). Hematite, chlorite, epidote, chalcedony, and opal show high surface abundances in the altered zones, while jarosite, biotite, and muscovite are lesser in the altered zones and they are mostly associated with specific lithological units in the study area. The DPCA image-maps of ASTER dataset show a little spatial dissimilarity with the ACE fraction images, especially in the DPCA4 image (Figures 7 and 12). High spatial similarity with fraction images was recorded in the LSU classification image-map (see Figure 9B). The overall accuracy and Kappa Coefficient calculated for the LSU classification image-maps derived from Landsat-8 versus the ACE fraction images derived from VINR + SWIR bands of ASTER were 76.25% and 0.64, respectively (see Table 6). The overall accuracy of 65.66% and Kappa Coefficient of 0.57 were assessed for the ASTER LSU classification image-maps (see Table 7). Using ASTER datasets, muscovite/kaolinite was intensely mapped compared to hematite/jarosite, chlorite/epidote, chalcedony/opal, and biotite. On the other hand, spectral mixing for hematite/jarosite, chlorite/epidote, chalcedony/opal, and biotite was more feasible.

The overall accuracy of 77% and Kappa Coefficient of 0.69 were calculated for the WV-3 LSU classification image-maps (see Table 8), which show a good potential for separating iron mineral classes. Subsequently, the virtual verification indicates that the alteration zones mapped by the Landsat-8, ASTER, and WV-3 datasets reveal a good rate of agreement (Kappa Coefficient of 0.57 to 0.69) and reasonable accuracy (overall accuracy of 65.66% to 77%), which could be pondered for prospecting Cu-Au mineralization. As a result, the boundaries between the Etah metamorphic and meta-igneous complex and sedimentary successions of the Franklinian Basin in the Central Terrane, orthogneiss in the northeastern part of the Cu-Au mineralization belt adjacent to Dallas Bugt, as well as the southern part of the Cu-Au mineralization belt nearby Marshall Bugt, can be considered as high potential zones for Cu-Au prospecting in the IMB.

6. Conclusions

Landsat-8, ASTER, and WV-3 multispectral remote sensing datasets were processed, interpreted, and integrated for mapping hydrothermal alteration minerals and prospecting Cu-Au mineralization in the IMB, Northwest Greenland. Iron oxides/hydroxide minerals and Al-OH, Mg-Fe-OH, CO_3 and Si-OH/SiO_2 alteration mineral groups were mapped by executing the DPCA, LSU, and ACE image processing techniques to the Landsat-8, ASTER, and WV-3 datasets. The discrimination of lithological units and the zones contain high concentration of iron oxides/hydroxide and clay minerals in the IMB were achieved using Landsat-8 data at the regional scale. The information extracted from Landsat-8 provides a synoptic view of alteration mineral zones in the IMB metallogenic province. Iron oxides/hydroxide minerals typically concentrated at the contact between sedimentary successions of the Franklinian Basin and Thule Supergroup with the Etah metamorphic and meta-igneous complex rocks. ASTER datasets helped to map the spatial distribution of Fe^{3+}/Fe^{2+} iron oxide/hydroxides, Al/Fe-OH, Mg-Fe-OH, Si-OH/SiO_2 mineral groups in the Cu-Au mineralization belt and surrounding areas, comprehensively. Fe^{3+}/Fe^{2+} iron oxide/hydroxides and Si-OH/SiO_2 were also detected in the contact between sedimentary successions and metamorphic and meta-igneous rocks, orthogneiss, and quartz diorite. Intense concentration of iron oxide/hydroxides and Si-OH/SiO_2 was identified within documented rust zones (Cu-Au mineralization).

Furthermore, fraction abundance of hematite, jarosite, biotite, muscovite, chlorite, epidote, chalcedony, and opal was detected in the Cu-Au mineralization belt and surrounding areas using the VNIR + SWIR bands of ASTER. Hence, the rust zones contain the assemblage of hematite/jarosite, chalcedony/opal, and chlorite/epidote with little amount of muscovite/kaolinite. Using the WV-3 dataset, Fe^{3+} and Fe^{2+} iron oxides and ferric and ferrous silicates were broadly mapped and discriminated in the southern part of the Cu-Au mineralization belt. High to moderate spatial distribution of Fe^{3+} and Fe^{2+} iron oxides and ferric silicates were detected in the rust zones. Strong fraction abundance of hematite, jarosite, and ferric silicates was also mapped in the rust zones. The virtual verification shows an appropriate overall accuracy and reasonable rate of agreement for

mapping alteration mineral zones using image processing techniques and remote sensing multispectral/multi-sensor satellite imagery. Consequently, high potential zones for Cu-Au prospecting were identified in the IMB, Northwest Greenland, including (i) the boundaries between the Etah metamorphic and meta-igneous complex rocks and sedimentary successions of the Franklinian Basin in the Central Terrane, (ii) orthogneiss in the northeastern part of the Cu-Au mineralization belt adjacent to Dallas Bugt, and (iii) the southern part of the Cu-Au mineralization belt nearby Marshall Bugt. It is recommended that these high prospective zones be considered for future comprehensive fieldwork and detailed geophysical and geochemical surveys in the IMB, Northwest Greenland. This investigation suggests the necessity of multispectral/multi-sensor satellite image processing analysis as a cost-effective tool for mining companies for reconnaissance stages of mineral prospecting before costly fieldwork, geophysical, and geochemical surveys in remote and inaccessible metallogenic provinces around the world.

References

1.　Pirajno, F.; Thomassen, B.; Iannelli, T.R.; Dawes, P.R. Copper—Gold mineralisation in Inglefield Land, NW Greenland. *Newsl. Int. Liaison Group Gold Miner.* **2000**, *30*, 49–53.

2.　Pirajno, P.; Thomassen, B.; Dawes, P.R. Copper–gold occurrences in the Palaeoproterozoic Inglefield mobile belt, northwest Greenland: A new mineralisation style? *Ore Geol. Rev.* **2003**, *22*, 225–249.

3.　Kolb, J.; Keiding, J.K.; Steenfelt, A.; Secher, K.; Keulen, N.; Rosa, D.; Stengaard, B.M. Metallogeny of Greenland. *Ore Geol. Rev.* **2016**, *78*, 493–555.

4.　Gabr, S.S.; Hassan, S.M.; Sadek, M.F. Prospecting for new gold-bearing alteration zones at El-Hoteib area, South Eastern Desert, Egypt, using remote sensing data analysis. *Ore Geol. Rev.* **2015**, *71*, 1–13.

5.　Amer, R.; El Mezayen, A.; Hasanein, M. ASTER spectral analysis for alteration minerals associated with gold mineralization. *Ore Geol. Rev.* **2016**, *75*, 239–251.

6.　Pour, A.B.; Park, Y.; Park, T.S.; Hong, J.K.; Hashim, M.; Woo, J.; Ayoobi, I. Evaluation of ICA and CEM algorithms with Landsat-8/ASTER data for geological mapping in inaccessible regions. *Geocarto Int.* **2018**, doi:10.1080/10106049.2018.1434684.

7.　Pour, A.B.; Park, Y.; Park, T.S.; Hong, J.K.; Hashim, M.; Woo, J.; Ayoobi, I. Regional geology mapping using satellite-based remote sensing approach in Northern Victoria Land, Antarctica. *Polar Sci.* **2018**, *16*, 23–46.

8.　Pour, A.B.; Park, T.S.; Park, Y.; Hong, J.K.; Zoheir, B.; Pradhan, B.; Ayoobi, I.; Hashim, M. Application of multi-sensor satellite data for exploration of Zn-Pb sulfide mineralization in the Franklinian Basin, North Greenland. *Remote Sens.* **2018**, *10*, 1186. doi:10.3390/rs10081186.

9.　Pour, A.B.; Hashim, M.; Park, Y.; Hong, J.K. Mapping alteration mineral zones and lithological units in Antarctic regions using spectral bands of ASTER remote sensing data. *Geocarto Int.* **2018**, *33*, 1281–1306.

10.　Testa, F.J.; Villanueva, C.; Cooke, D.R.; Zhang, L. Lithological and hydrothermal alteration mapping of epithermal, porphyry and tourmaline breccia districts in the Argentine Andes using ASTER imagery. *Remote Sens.* **2018**, *10*, 203. doi:10.3390/rs10020203.

11.　Sheikhrahimi, A.; Pour, B.A.; Pradhan, B.; Zoheir, B. Mapping hydrothermal alteration zones and lineaments associated with orogenic gold mineralization using ASTER remote sensing data: A case study from the Sanandaj-Sirjan Zone, Iran. *Adv. Space Res.* **2019**, *63*, 3315–3332.

12.　Noori, L.; Pour, B.A.; Askari, G.; Taghipour, N.; Pradhan, B.; Lee, C.-W.; Honarmand, M. Comparison of Different Algorithms to Map Hydrothermal Alteration Zones Using ASTER Remote Sensing Data for Polymetallic Vein-Type Ore Exploration: Toroud–Chahshirin Magmatic Belt (TCMB), North Iran. *Remote Sens.* **2019**, *11*, 495. doi:10.3390/rs11050495.

13. Rajendran, S.; Nasir, S. Characterization of ASTER spectral bands for mapping of alteration zones of volcanogenic massive sulphide deposits. *Ore Geol. Rev.* **2017**, *88*, 317–335.

14. Salehi, T.; Tangestani, M.H. Large-scale mapping of iron oxide and hydroxide minerals of Zefreh porphyry copper deposit, using Worldview-3 VNIR data in the Northeastern Isfahan, Iran. *Int. J. Appl. Earth Obs. Geoinf.* **2018**, *73*, 156–169.

15. Pour, A.B.; Hashim, M.; Hong, J.K.; Park, Y. Lithological and alteration mineral mapping in poorly exposed lithologies using Landsat-8 and ASTER satellite data: North-eastern Graham Land, Antarctic Peninsula. *Ore Geol. Rev.* **2019**, *108*, 112–133.

16. Pour, A.B.; Park, Y.; Crispini, L.; Läufer, A.; Hong, J.K.; Park, T.-Y.S.; Zoheir, B.; Pradhan, B.; Muslim, A.M.; Hossain, M.S.; et al. Mapping Listvenite Occurrences in the Damage Zones of Northern Victoria Land, Antarctica Using ASTER Satellite Remote Sensing Data. *Remote Sens.* **2019**, *11*, 1408. doi.org/10.3390/rs11121408.

17. Safari, M.; Maghsodi, A.; Pour, A.B. Application of Landsat-8 and ASTER satellite remote sensing data for porphyry copper exploration: A case study from Shahr-e-Babak, Kerman, south of Iran. *Geocarto Int.* **2018**, *33*, 1186–1201.

18. Ninomiya, Y.; Fu, B. Thermal infrared multispectral remote sensing of lithology and mineralogy based on spectral properties of materials. *Ore Geol. Rev.* **2019**, *108*, 54–72.

19. Bedini, E. Application of WorldView-3 imagery and ASTER TIR data to map alteration minerals associated with the Rodalquilar gold deposits, southeast Spain. *Adv. Space Res.* **2019**, *63*, 3346–3357.

20. Sun, L.; Khan, S.; Shabestari, P. Integrated Hyperspectral and Geochemical Study of Sediment-Hosted Disseminated Gold at the Goldstrike District, Utah. *Remote Sens.* **2019**, *11*, 1987. doi:10.3390/rs11171987.

21. Zoheir, B.; Emam, A.; Abdel-Wahed, M.; Soliman, N. Multispectral and Radar Data for the Setting of Gold Mineralization in the South Eastern Desert, Egypt. *Remote Sens.* **2019**, *11*, 1450. doi:10.3390/rs11121450.

22. Zoheir, B.; El-Wahed, M.A.; Pour, A.B.; Abdelnasser, A. Orogenic Gold in Transpression and Transtension Zones: Field and Remote Sensing Studies of the Barramiya–Mueilha Sector, Egypt. *Remote Sens.* **2019**, *11*, 2122. doi:10.3390/rs11182122.

23. Leverington, D.W.; Moon, W.M. Landsat-TM-Based discrimination of Lithological units associated with the Purtuniq ophiolite, Quebec, Canada. *Remote Sens.* **2012**, *4*, 1208–1231.

24. He, J.; Harris, J.R.; Sawada, M.; Behnia, P. A comparison of classification algorithms using Landsat-7 and Landsat-8 data for mapping lithology in Canada's Arctic. *Int. J. Remote Sens.* **2015**, *36*, 2252–2276.

25. Pour, B.A.; Hashim, M.; Marghany, M. Exploration of gold mineralization in a tropical region using Earth Observing-1 (EO1) and JERS-1 SAR data: A case study from Bau gold field, Sarawak, Malaysia. *Arabian J. Geosci.* **2014**, *7*, 2393–2406.

26. Pour, B.A.; Hashim, M.; van Genderen, J. Detection of hydrothermal alteration zones in a tropical region using satellite remote sensing data: Bau gold field, Sarawak, Malaysia. *Ore Geol. Rev.* **2013**, *54*, 181–196.

27. Askari, G.; Pour, A.B.; Pradhan, B.; Sarfi, M.; Nazemnejad, F. Band Ratios Matrix Transformation (BRMT): A Sedimentary Lithology Mapping Approach Using ASTER Satellite Sensor. *Sensors* **2018**, *18*, 3213. doi:10.3390/s18103213.

28. Kurata, K.; Yamaguchi, Y. Integration and Visualization of Mineralogical and Topographical Information Derived from ASTER and DEM data. *Remote Sens.* **2019**, *11*, 162. doi:10.3390/rs11020162.

29. Guha, A.; Yamaguchi, Y.; Chatterjee, S.; Rani, K.; Vinod Kumar, K. Emittance Spectroscopy and Broadband Thermal Remote Sensing Applied to Phosphorite and Its Utility in Geoexploration: A Study in the Parts of Rajasthan, India. *Remote Sens.* **2019**, *11*, 1003. doi:10.3390/rs11091003.

30. Irons, J.R.; Dwyer, J.L.; Barsi, J.A. The next Landsat satellite: The Landsat Data Continuity Mission. *Remote Sens. Environ.* **2012**, *145*, 154–172.

31. Roy, D.P.; Wulder, M.A.; Loveland, T.A.; Woodcock, C.E.; Allen, R.G.; Anderson, M.C.; Helder, D.; Irons, J.R.; Johnson, D.M.; Kennedy, R.; et al. Landsat-8: Science and product vision for terrestrial global change research. *Remote Sens. Environ.* **2014**, *145*, 154–172.

32. Bhambri, R.; Bolch, T.; Chaujar, R.K. Mapping of debris-covered glaciers in the Garhwal Himalayas using ASTER DEMs and thermal data. *Int. J. Remote Sens.* **2011**, *32*, 8095–8119.

33. Shukla, A.; Arora, M.K.; Gupta, R.P. Synergistic approach for mapping debris-covered glaciers using optical–thermal remote sensing data with inputs from geomorphometric parameters. *Remote Sens. Environ.* **2010**, *114*, 1378–1387.

34. Abrams, M.; and Hook, S.J. Simulated ASTER data for geologic studies. *IEEE Trans. Geosci. Remote Sens.* **1995**, *33*, 692–699.

35. Hunt, G.R.; Ashley, R.P. Spectra of altered rocks in the visible and near-infrared. *Econ. Geol.* **1979**, *74*, 1613–1629.

36. Clark, R.N. Spectroscopy of rocks and minerals, and principles of spectroscopy. In *Manual of Remote Sensing*; Rencz, A., Ed.; Wiley and Sons Inc.: New York, NY, USA, 1999; Volume 3, pp. 3–58.

37. Cloutis, E.A.; Hawthorne, F.C.; Mertzman, S.A.; Krenn, K.; Craig, M.A.; Marcino, D.; Methot, M.; Strong, J.; Mustard, J.F.; Blaney, D.L.; Detection and discrimination of sulfate minerals using reflectance spectroscopy. *Icarus* **2006**, *184*, 121–157.

38. Salisbury, J.W.; D'Aria, D.M. Emissivity of terrestrial material in the 8–14 μm atmospheric window. *Remote Sens. Environ.* **1992**, *42*, 83–106.

39. Salisbury, J.W.; Walter, L.S. Thermal infrared (2.5–13.5 μm) spectroscopic remote sensing of igneous rock types on particulate planetary surfaces. *J. Geophys. Res.* **1989**, *94*, 9192–9202.

40. Ninomiya, Y. Quantitative estimation of SiO_2 content in igneous rocks using thermal infrared spectra with a neural network approach. *IEEE TGRS* **1995**, *33*, 684–691.

41. Ninomiya, Y.; Fu, B. Regional lithological mapping using ASTER-TIR data: Case study for the Tibetan Plateau and the surrounding area. *Geosciences*, **2016**, *6*, 39. doi:10.3390/geosciences6030039.

42. DigitalGlobe. WorldView-3 Datasheet. 2014. Available online: https://www.digitalglobe.com/sites/default/files/DG_WorldView3_DS_forWeb_0.pdf (accessed on 7 September 2019).

43. Kruse, F.; Perry, S. Mineral mapping using simulated Worldview-3 short-wave infrared imagery. *Remote Sens.* **2013**, *5*, 2688–2703.

44. Kruse, F.A.; Baugh, M.W.; Perry, S.L. Validation of DigitalGlobe Worldview-3 earth imaging satellite shortwave infrared bands for mineral mapping. *J. Appl. Remote Sens.* **2015**, *9*, 1–18.

45. Asadzadeh, S.; Filho, C.R.S. Investigating the capability of WorldView-3 superspectral data for direct hydrocarbon detection. *Remote Sens. Environ.* **2016**, *173*, 162–173.

46. Mars, J.C. Mineral and Lithologic Mapping Capability of WorldView 3 Data at Mountain Pass, California, Using True- and False-Color Composite Images, Band Ratios, and Logical Operator Algorithms. *Econ. Geol.* **2018**, *113*, 1587–1601.

47. Sun, Y.; Tian, S.; Di, B. Extracting mineral alteration information using Worldview-3 data. *Geosci. Front.* **2017**, *8*, 1051–1062.

48. Ye, B.; Tian, S.H.; Ge, J.; Sun, Y. Assessment of WorldView-3 data for lithological mapping. *Remote Sens.* **2017**, *9*, 1132.

49. Dawes, P.R.; Frisch, T.; Garde, A.A.; Iannelli, T.R.; Ineson, J.R.; Pirajno, F.; Sønderholm, M.; Stemmerik, L.; Stouge, S.; Thomassen, B.; et al. Kane Basin 1999: Mapping, stratigraphic studies and economic assessment of Precambrian and Lower Palaeozoic provinces in North-West Greenland. *Geol. Greenl. Survey Bull.* **2000**, *186*, 11–28.

50. Thomassen, B.; Dawes, P.R.; Iannelli, T.R.; Pirajno, F. *Gold Indications in Northern Inglefield Land, North-West Greenland: A Preliminary Report from Project Kane Basin 1999*; the Geological Survey of Denmark and Greenland (GEUS): Copenhagen, Denmark, 2000; 14p.

51. Thomassen, B.; Pirajno, F.; Iannelli, T.R.; Dawes, P.R.; Jensen, S.M. *Economic Geology Investigations in Inglefield Land, North–West Greenland: Part of the Project Kane Basin 1999*; the Geological Survey of Denmark and Greenland (GEUS): Copenhagen, Denmark, 2000; 98p.

52. Schjøth, F.; Steenfelt, A.; Thorning, L. (Eds.) *Regional Compilations of Geoscience Data from Inglefield Land, North-West Greenland*; the Geological Survey of Denmark and Greenland (GEUS): Copenhagen, Denmark, 1996; 35p.

53. Schjøth, F.; Thorning, L. *GIS Compilation of Geoscience Data: An ArcView GIS Version of Previously Published Thematic Maps from Inglefield Land*; the Geological Survey of Denmark and Greenland (GEUS): Copenhagen, Denmark, 1998; 59p.

54. Dawes, P.R. *Explanatory Notes to the Geological Map of Greenland, 1:500,000, Thule, Sheet 5, Map Series 2*; Geological Survey of Denmark and Greenland: Copenhagen, Denmark, 2006.

55. Dawes, P.R. *Explanatory Notes to the Geological Map of Greenland, 1:500,000, Humboldt Gletscher, Sheet 6, Map Series 1*; Geological Survey of Denmark and Greenland: Copenhagen, Denmark, 2004.

56. Nutman, A.P.; Dawes, P.R.; Kalsbeek, F.; Hamilton, M.A. Palaeoproterozoic and Archaean gneiss complexes in northern Greenland: Palaeoproterozoic terrane assembly in the High Arctic. *Precambrian Res.* **2008**, *161*, 419–451.

57. Dawes, P.R.; Larsen, O.; Kalsbeek, F. Archaean and Proterozoic crust in North-West Greenland: Evidence from Rb–Sr whole-rock age determinations. *Can. J. Earth Sci.* **1988**, *25*, 1365–1373.

58. Dawes, P.R. *A Review of Geoscientific Exploration and Geology in the Kane Basin Region of Greenland, Central Nares Strait*; the Geological Survey of Denmark and Greenland (GEUS): Copenhagen, Denmark, 1999; 63p.

59. Henriksen, N.; Higgins, A.K.; Kalsbeek, F.; Pulvertaft, T.C.R. Greenland from Archaean to Quaternary: Descriptive text to the geological map of Greenland 1:2,500,000. *Geol. Greenl. Survey Bull.* **2000**, *185*, 93.

60. Higgins, A.K.; Ineson, J.R.; Peel, J.S.; Surlyk, F.; Sønderholm, M. Lower Palaeozoic Franklinian Basin of North Greenland. In *Sedimentary Basins of North Greenland*; Peel, J.S., Sønderholm, M., Eds.; Bulletin-Grønlands Geologiske Undersøgelse; 1991; Volume 160, pp. 71–139.

61. Thomassen, B.; Appel, P.W. *Ground Check of Airborne Anomalies and Regional Rust Zones in Inglefield Land, North-West Greenland*; Rapport-Danmarks og Grønlands Geologiske Undersøgelse; 1997; 43p.

62. Thompson, A.B. Some aspects of fluid motion during metamorphism. *J. Geol. Soc.* **1987**, *144*, 309–312.

63. Abrams, M.; Hook, S.; Ramachandran, B. *ASTER User Handbook*, Version 2; Jet Propulsion Laboratory, California Institute of Technology: 2004. Available online: http://asterweb.jpl.nasa.gov/content/03_data/04_Documents/aster_guide_v2.pdf (accessed on 7 September 2019).

64. Kuester, M. *Radiometric Use of WV-3 Imagery*; Technical Note; 2016; p. 12.

65. Kuester, M.A.; Ochoa, M.; Dayer, A.; Levin, J.; Aaron, D.; Helder, D.L.; Leigh, L.; Czapla-Meyers, J.; Anderson, N.; Bader, B.; et al. *Absolute Radiometric Calibration of the DigitalGlobe Fleet and Updates on the New WV-3 Sensor Suite*; Technical Note; 2015; p. 16.

66. Iwasaki, A.; Tonooka, H. Validation of a crosstalk correction algorithm for ASTER/SWIR. *IEEE Trans. Geosci. Remote Sens.* **2005**, *43*, 2747–2751.

67. Cooley, T.; Anderson, G.P.; Felde, G.W.; Hoke, M.L.; Ratkowski, A.J.; Chetwynd, J.H.; Gardner, J.A.; Adler-Golden, S.M.; Matthew, M.W.; Berk, A.; et al. FLAASH, a MODTRAN4-based atmospheric correction algorithm, its application and validation. In Proceedings of the IEEE International on Geoscience and Remote Sensing Symposium, Toronto, Ontario, Canada 2002; Volume 3, pp. 1414–1418.

68. Research Systems, Inc. *ENVI Tutorials*; Research Systems, Inc.: Boulder, CO, USA, 2008.

69. Fraser, S.J.; Green, A.A. A software defoliant for geological analysis of band ratios. *Int. J. Remote Sens.* **1987**, *8*, 525–532.

70. Crosta, A.; Moore, J. Enhancement of Landsat Thematic Mapper imagery for residual soil mapping in SW Minais Gerais State, Brazil: A prospecting case history in Greenstone belt terrain. In Proceedings of the 7th ERIM Thematic Conference: Remote Sensing for Exploration Geology, Calgary, AB, Canada, 2–6 October 1989; pp. 1173–1187.

71. Crosta, A.P.; Souza Filho, C.R.; Azevedo, F.; Brodie, C. Targeting key alteration minerals in epithermal deposits in Patagonia, Argentina, Using ASTER imagery and principal component analysis. *Int. J. Remote Sens.* **2003**, *24*, 4233–4240.

72. Loughlin, W.P. Principal components analysis for alteration mapping. *Photogramm. Eng. Remote Sens.* **1991**, *57*, 1163–1169.

73. Kokaly, R.F.; Clark, R.N.; Swayze, G.A.; Livo, K.E.; Hoefen, T.M.; Pearson, N.C.; Wise, R.A.; Benzel, W.M.; Lowers, H.A.; Driscoll, R.L.; et al. USGS Spectral Library Version 7: U.S. *Geol. Survey Data Ser.* **2017**. 1035, 61. doi:10.3133/ds1035.

74. van der Werff, H.; van der Meer, F. Sentinel-2A MSI and Landsat 8 OLI Provide Data Continuity for Geological Remote Sensing. *Remote Sens.* **2016**, *8*, 883. doi:10.3390/rs8110883.

75. Clark, R.N.; Swayze, G.A.; Gallagher, A.; King, T.V.V.; Calvin, W.M. *The U.S. Geological Survey, Digital Spectral Library: Version 1: 0.2 to 3.0 Microns: U.S. Geological Survey Open File Report 93-592*; 1993; 1340p. Available online: http://speclab.cr.usgs.gov (accessed on 24 August 1999).

76. Clark, R.N.; Swayze, G.A. Mapping minerals, amorphous materials, environmental materials, vegetation, water, ice, and snow, and other materials. In Proceedings of the USGS Tricorder Algorithm, Summaries of the Fifth Annual JPL Airborne Earth Science Workshop, The United States Geological Survey, Reston, VA, USA, 3 August 1995.

77. Kalinowski, A.; Oliver, S. *ASTER Mineral Index Processing Manual*; Technical Report; Geoscience Australia: Canberra, Australia, 2004. Available online: http://www.ga.gov.au/image_cache/GA7833.pdf (accessed on 12 August 2018).

78. Crowley, J.K.; Brickey, D.W.; Rowan, L.C. Airborne imaging spectrometer data of the Ruby Mountains, Montana: Mineral discrimination using relative absorption band-depth images. *Remote Sens. Environ.* **1989**, *29*, 121–134.

79. Ninomiya, Y.; Fu, B.; Cudahy, T.J. Detecting lithology with Advanced Spaceborne Thermal Emission and Reflection Radiometer (ASTER) multispectral thermal infrared radiance-at-sensor data. *Remote Sens. Environ.* **2005**, *99*, 127–139.

80. Boardman, J.W. Inversion of imaging spectrometry data using singular value decomposition. In Proceedings of the IGARSS'89, 12th Canadian Symposium on Remote Sensing, Vancouver, Canada, 10–14 July 1989; Volume 4, pp. 2069–2072.

81. Boardman, J.W. Sedimentary Facies Analysis Using Imaging Spectrometry: A Geophysical Inverse Problem. Unpublished Ph. D. Thesis, University of Colorado, Boulder, CO, USA, 1992; p. 212.

82. Adams, J.B.; Smith, M.O.; Gillespie, A.R. Imaging spectroscopy: Interpretation based on spectral mixture analysis. In *Remote Geochemical Analysis: Elemental and Mineralogical Composition*; Pieters, C.M., Englert, P.A.J., Eds.; Cambridge University Press: New York, NY, USA, 1993; pp. 145–166.

83. Adams, J.B.; Sabol, D.E.; Kapos, V.; Filho, R.A.; Roberts, D.A.; Smith, M.O.; Gillespie, A.R. Classification of multispectral images based on fractions of endmembers: Application to land-cover change in the Brazilian Amazon. *Remote Sens. Environ.* **1995**, *52*, 137–154.

84. Kruse, F.A.; Bordman, J.W.; Huntington, J.F. Comparison of airborne hyperspectral data and EO-1 Hyperion for mineral mapping. *IEEE Trans. Geosci. Remote Sens.* **2003**, *41*, 1388–1400.

85. Kruse, F.A.; Perry, S.L. Regional mineral mapping by extending hyperspectral signatures using multispectral data. *IEEE Trans. Geosci. Remote Sens.* **2007**, *4*, 154–172.

86. Boardman, J.W.; Kruse, F.A. Automated spectral analysis: A geologic example using AVIRIS data, north Grapevine Mountains, Nevada. In Proceedings of the Tenth Thematic Conference on Geologic Remote Sensing, Environmental Research Institute of Michigan, Ann Arbor, MI, USA, 9 June 1994; pp. I-407–I-418.

87. Boardman, J.W.; Kruse, F.A.; Green, R.O. Mapping target signatures via partial unmixing of AVIRIS data. In Proceedings of the Fifth JPL Airborne Earth Science Workshop, Pasadena, CA, USA,12 March 1995; Volume 1, pp. 23–26.

88. Clark, R.N. Spectroscopy of rocks and minerals, and principles of spectroscopy. In *Manual of Remote Sensing*; Rencz, A., Ed.; Wiley and Sons Inc.: New York, NY, USA, 1999; Volume 3, pp. 3–58.

89. Manolakis, D.; Marden, D.; Shaw, G.A. Hyperspectral Image Processing for Automatic Target Detection Applications. *Linc. Lab. J.* **2003**, *14*, 79–116.

90. Kraut, S.; Scharf, L.L.; Butler, R.W. The adaptive coherence estimator: A uniformly most-powerful-invariant adaptive detection statistic. *IEEE Trans. Signal Process.* **2005**, *53*, 427–438.

91. Bidon, S.; Besson, O.; Tourneret, J.Y. The Adaptive Coherence Estimator is the Generalized Likelihood Ratio Test for a Class of Heterogeneous Environments. *IEEE Signal Process. Lett.* **2008**, *15*, 281–284.

92. Kraut, S.; Scharf, L.L.; McWhorter, L.T. Adaptive subspace detectors. *IEEE Trans. Signal Process.* **2001**, *49*, 1–16.

93. Alvey, B.; Zare, A.; Cook, M.; Ho, D.K.C. Adaptive coherence estimator (ACE) for explosive hazard detection using wideband electromagnetic induction (WEMI). In Proceedings of the SPIE 9823, Detection and Sensing of Mines, Explosive Objects, and Obscured Targets XXI, Baltimore, MA, USA, 3 May 2016. doi:10.1117/12.2223347.

94. Warren, S.G. Optical properties of snow. *Rev. Geophys. Space Phys.* **1982**, *20*, 67–89.

95. Hall, D.K.; Riggs, G.A.; Salomonson, V.V.; DiGirolamo, N.E.; Bayr, K. MODIS snow-cover products. *Remote Sens. Environ.* **2002**, *83*, 181–1194.

96. Gupta, R.P.; Haritashya, U.K.; Singh, P. Mapping dry/wet snow cover in the Indian Himalayas using IRS multispectral imagery. *Remote Sens. Environ.* **2005**, *97*, 458–469.

97. Pour, B.A.; Hashim, M. Identification of hydrothermal alteration minerals for exploring of porphyry copper deposit using ASTER data, SE Iran. *J. Asian Earth Sci.* **2011**, *42*, 1309–1323.

98. Velosky, J.C.; Stern, R.J.; Johnson, P.R. Geological control of massive sulfide mineralization in the Neoproterozoic Wadi Bidah shear zone, southwestern Saudi Arabia, inferences from orbital remote sensing and field studies. *Precambrian Res.* **2003**, *123*, 235–247.

99. Bishop, J.L.; Lane, M.D.; Dyar, M.D.; Brwon, A.J. Reflectance and emission spectroscopy study of four groups of phyllosilicates: Smectites, kaolinite-serpentines, chlorites and micas. *Clay Min.* **2008**, *43*, 35–54.

100. Sherman, D.M.; Waite, T.D. Electronic spectra of Fe^{3+} oxides and oxide-hydroxides in the near IR to near UV. *Am. Mineral.* **1985**, *70*, 1262–1269.

101. Morris, R.V.; Lauer, H.V.; Lawson, C.A.; Girson, E.K.; Nace, G.A.; Stewart, C. Spectral and other physicochemical properties of submicron powders of hematite (á-Fe_2O_3), maghemite (ã-Fe_2O_3), magnetite ($Fe3O4$), goethite (á-$FeOOH$), and lepidocrocite (ã-$FeOOH$). *J. Geophys. Res.* **1985**, *90*, 3126–3144.

102. Story, M.; Congalton, R. Accuracy assessment: A user's perspective. *Photogramm. Eng. Remote Sens.* **1986**, *52*, 397–399.

103. Congalton, R.G. A review of assessing the accuracy of classification of remotely sensed data. *Remote Sens. Environ.* **1991**, *37*, 35–46.

104. Lillesand, T.; Kiefer, R. *Remote Sensing and Image Interpretation*; John Wiley & Sons, Inc.: New York, NY, USA, 1994; Chapter 7.

105. Steenfelt, A.; Dam, E. *Reconnaissance Geochemical Mapping of Inglefield Land, North-West Greenland*; Rapport-Danmarks og Grønlands Geologiske Undersøgelse; 1996; 27p.

106. Bedini, E. Mapping lithology of the Sarfartoq carbonatite complex, southern West Greenland, using HyMap imaging spectrometer data. *Remote Sens. Environ.* **2009**, *113*, 1208–1219.

107. Bedini, E.; Rasmussen, T.M. Use of airborne hyperspectral and gamma-ray spectroscopy data for mineral exploration at the Sarfartoq carbonatite complex, southern West Greenland. *Geosci. J.* **2018**, *22*, 641–651.

108. Bedini, E. Mineral mapping in the Kap Simpson complex, central East Greenland, using HyMap and ASTER remote sensing data. *Adv. Space Res.* **2011**, *47*, 60–73.